Characterization of a Low Current LaB_6 Heaterless Hollow Cathode with Krypton Propellant

Prachi Jain

Thesis submitted to the Faculty of the
Virginia Polytechnic Institute and State University
in partial fulfillment of the requirements for the degree of

Master of Science
in
Aerospace Engineering

Colin S. Adams, Chair
Bhuvana Srinivasan
Gregory D. Earle

May 21, 2020
Blacksburg, Virginia

Keywords: Electric Propulsion, Hollow Cathode, Krypton, Lanthanum hexaboride

Characterization of a Low Current LaB_6 Heaterless Hollow Cathode with Krypton Propellant

Prachi Jain

ABSTRACT

A first-generation LaB_6 heaterless hollow cathode with a flat-plate anode is experimentally investigated. The cathode is characterized using krypton as propellant at varying flow rates, discharge currents and cathode-anode distances. Voltage probes, used to make direct voltage measurements in the ignition circuit, are the only diagnostic tool used experimentally. A plasma model is used to infer plasma parameters in the cathode emitter region. The cathode characterization results are consistent with those obtained during previous investigations of 1 A-class LaB_6 hollow cathode with krypton. A peak-to-peak anode voltage criterion is used to identify the discharge modes and the occurrence of mode transition. Fourier analysis of the keeper and anode voltage waveforms carried out to study the discharge mode behavior reveals resonant frequencies ranging from 40 to 150 kHz. Lastly, post-test visual observations of the cathode components show signs of emitter poisoning and keeper erosion.

Characterization of a Low Current LaB_6 Heaterless Hollow Cathode with Krypton Propellant

Prachi Jain

GENERAL AUDIENCE ABSTRACT

Recent years have seen rapid growth in the development of both stand-alone satellites and satellite constellations. A critical component of these satellites is the on-board propulsion system, which is responsible for controlling their orientation with respect to the object of interest and keeping the spacecraft in the assigned orbit. Generally, electric propulsion systems are used for this purpose. These types of propulsion systems use electrical power to change the velocity of satellite, providing a small thrust for a long duration of time as compared to chemical propulsion systems.

Certain types of electric thrusters utilize a hollow cathode device as an electron source to start-off and support the thruster operation. In this research, a non-conventional hollow cathode for low power applications is developed and tested. The main characteristic of the developed cathode is the heaterless configuration, which eliminates the heater module used in conventional cathodes to enable the cathode to reach its operational temperature. The absence of a heater reduces the complexity of the cathode and the electrical power system. The cathode utilizes an electron emitter material which is insensitive to impurities and air exposure. Additionally, unlike typical electric thrusters which use xenon as the fuel, this cathode uses krypton which is similar to xenon but is less expensive.

The presented work includes an overview of electric propulsion and the hollow cathode operation, followed by a detailed discussion of the heaterless hollow cathode design, the experimental setup and the test results. Several noteworthy findings regarding cathode operation are included as well. This research shows that the non-conventional heaterless hollow cathode and its operation with krypton have the potential to improve the overall thruster performance by reducing the weight and the cost, thus contributing to an integral aspect of satellite on-board propulsion.

This work is dedicated to Kalpana Chawla,
who proved that the path from dreams to success does exist.
Thank you for inspiring me.

Acknowledgments

I consider myself privileged to have met and learnt from all the people during my Master's journey. I truly would not have succeeded without the encouragement and support of all the people mentioned below and many more.

Firstly, I would like to convey my heartfelt appreciation to my advisor, Dr. Colin Adams, who has guided and encouraged me throughout graduate school. His patience, and immense practical and theoretical knowledge have been a catalyst for my research. I would like to also thank Dr. Bhuvana Srinivasan and Dr. Gregory Earle for reviewing my thesis and their feedback.

My deepest gratitude goes to Alex Nikrant, who laid the foundations for Electric propulsion related experimental capabilities at Virginia Tech. His passion for electric propulsion technology has inspired me to follow his footsteps. I appreciate his timely advice and response even after graduation.

I thank my fellow labmates at Space@VT for the interesting discussions on everything ranging from research to memes, and for all the fun we have had in the past two years. I am also indebted to my fellow graduate students who spent long hours in the lab with me, ensuring the experiments were conducted smoothly. I could not have asked for a better cohort.

Additionally, I would like to recognize the invaluable assistance provided by Dr. Carolina Tallon and Kevin Gjata, of the Materials Science and Engineering department at Virginia Tech, for baking the graphite parts in their vacuum furnace. Special thanks to Dr. Richard Branam and Matthew Warren of the University of Alabama for providing a copy of their thesis and answering my questions.

Last but not the least, I would like to thank my family: my parents and my sister for constantly believing in me and encouraging me when the skies were gray.

Contents

List of Figures

List of Tables

Nomenclature

α	material-specific constant
$\triangle v$	change in velocity required for maneuvering
$\dot{m}_i$	ion flow rate
η_m	mass utilization efficiency
γ	total thrust correction
λ_i	ionization mean free path
$\ln \Lambda$	coulomb logarithm
ω_c	electron cyclotron frequency
Ω_e	electron Hall parameter
ϕ_0	classical work function
ϕ_s	cathode sheath voltage
ϕ_{wf}	corrected work function
A_g	active grid area
A_t	thruster channel area
E_s	sheath electric field
I_b	beam current
I_d	cathode discharge current
I_e	electron current

I_i ion current

I_r random electron flux at sheath edge

I_t thermionic electric current

I_{max} maximum extracted ion current

J_b normalized thermionic emission current

J_i infalling ion current

J_r random electron current

J_{max} maximum Child-Langmuir current density

J_{th} thermionic emission current

m_e electron mass

m_f required fuel mass

m_i ion mass

m_p propellant mass

m_{ip} ionized propellant mass

m_{PL} final Payload mass

n_a neutral density

r_e plasma radius

r_L electron Larmor radius

T_w wall temperature, K

T_{eV} electron temperature, eV

U^+ ionization potential

v_a neutral velocity

V_b net beam voltage

v_i	ion velocity
V_{ea}	emitter-anode voltage
V_{ek}	emitter-keeper voltage
v_{ex}	propellant exhaust velocity
A	plasma attachment area
B	magnetic field strength
D	Richardson-Dushmann coefficient
d	effective grid separation
E	electric field at the emitter surface
e	electron charge
g	acceleration due to gravity
Isp	specific impulse
J	thermionic emission current density
k	Boltzmann's constant
L	thruster channel length, plasma length
M	propellant ion mass
R	plasma resistance
T	temperature, K
T	thrust
V	applied grid voltage
v	collision frequency
Z	charge state of plasma

Chapter 1

Introduction

1.1 Motivation

Recently, small satellites have transformed the space industry. The momentous period after World War II was dominated solely by government space agencies due to high mass of a spacecraft or satellites, which eventually led to high launch cost. CubeSat and Nanosatellite technologies have reduced the entry capital barrier to the satellite industry, thus allowing private companies, start-ups and universities to contribute. Launch providers have supported this advancement by offering low cost secondary payload rides. Small satellites missions for telecommunication, data gathering, surveillance, defense, navigation, radio relays, and agriculture have gained traction. For instance, companies like SpaceX and Oneweb have launched numerous batches of satellites for their space internet mega constellation plan. Starting 2018, small satellites have begun to venture out of the earth orbit into interplanetary space. Several robotic and deep space missions with small satellites as long-life probes to planets, asteroids, comets, etc are in development. This global interest in exploring the cosmos to extend human presence throughout the solar system and beyond requires advanced, resilient and long-life technology to sustain the extreme environment in space, improve approach navigation and ensure reliable landing.

The long life of these missions also demands a high endurance propulsion system. While chemical propulsion systems are sufficient to launch payloads from Earth's surface to the desired orbit, in-space propulsion demands a different type of propulsion system for altitude control, precision pointing, orbital maneuvering, or deep space travel. For this purpose, electric propulsion (EP) systems are utilized due to their suitability to long duration missions. Any propulsion system that utilizes electrical energy to increase the propellant exhaust velocity is an EP system. Unlike a chemical propulsion system, which is limited by its propellant carrying capacity, an EP system is

limited by the available electric power. However, an EP system with an external power source or a renewable power source eliminates this limitation.

Scaling down the propulsion system reduces both power and mass of the system, which may lead to enhanced payload capabilities and lower launch costs. Thus, it is evident that there is an increased interest in small spacecraft missions. Ion and Hall thrusters are some of the popular EP technologies that are currently being developed at a tremendous pace. Most of these systems use xenon as the propellant because of its high atomic mass compared to other inert gases. Recently, many private companies have successfully involved themselves with research and development of other cheaper and readily available propellants such as iodine, krypton, argon, and water.

Both gridded ion and Hall thrusters, utilize an electron source to initiate the discharge and neutralize the thruster plume (see Section 2.1). A hollow cathode device, which utilizes minimal electric power and propellant to form a cathode plasma, is used as an electron source for these purposes. Consequently, the cathode affects the performance and life of the thrusters to a great extent. The most common reason for cathode failure is the heater, which heats up the electron emitter to allow it to thermionically emit electrons for successful operation. Therefore, a heaterless hollow cathode ensures a reliable system, decreases the power requirement as well as reduces the cathode start-up time.

Low power hollow cathode operation poses significant challenges. A reliable heating system, high power efficiency, low propellant utilization, and the unpredictable cathode behavior are some of the challenges that are currently being dealt with in the research community. These challenges must be overcome to enable the use of EP technology for long term missions and deep space travel.

1.2 Research focus and objectives

The presented research aims to characterize the performance of the previously developed low power, heaterless hollow cathode, referred to as the VTHHC, with a lanthanum hexaboride (LaB_6) emitter and krypton propellant. The objectives of the research are as follows:

- Improve the experimental test setup based on observations from previous VTHHC tests with argon gas as the propellant.
- Characterize and assess the performance of the VTHHC. Determine the operational range of discharge current and flow rates.
- Observe and comment on the transition of the cathode plume between different modes to

contribute to the generalized framework of heaterless hollow cathode's unpredictable behavior.

- Observe and comment on the influence of anode position on the VTHHC discharge characteristics.
- Compare the VTHHC performance with argon and krypton as propellant.

The following chapters address the significance of the ideas explored in this research, related work done previously, the adopted methodology and experimental setup to conduct the experiment, results obtained, and the conclusions drawn from these results.

Chapter 2

Background

Challenged and inspired by science fiction novels like Jules Verne's "From the Earth to the Moon" and many others, young visionaries in the late 1800s set out to pave a path to space and beyond. One such brilliant scientist, Tsiolkovsky, wrote the article "Investigation of Universal Space by means of Reactive Devices" which contains the famous Tsiolkovsky Rocket Equation. In one form, this equation is given by [1]

$$m_f = m_{PL}\,(e^{\triangle v/v_e x} - 1). \tag{2.1}$$

This equation establishes that a device can accelerate itself using thrust by expelling a fraction of its mass at high velocity, in accordance with the law of conservation of momentum. Eight years later in 1911, Tsiolkovsky mentioned the idea of EP in a published article. In 1906, Robert Goddard independently probed the idea of EP in U.S.

Choueiri [5] published a review of the history of EP up to the 1950s, and information on developments in EP thereafter can be found in reference books [6] and websites [7]. Figure 2.1 shows the timeline of important events in the history of EP from 1906 to 1933.

In spite of their initial interests and explorations in the field of EP, Tsiolkovsky and Goddard deemed EP as an impractical technology and dedicated themselves to chemical propulsion. The onset of World War II led to a hiatus in the development of the idea of EP because it had no relevance to military applications, and vacuum simulation was not within the reach of most laboratories. Effort was put into bringing chemical propulsion to reality. The year of 1949 saw the re-emergence of EP. Figure 2.2 highlights important events from 1949 to 2004.

Shepherd and Cleaver's proof of concept study revealed the need of a propellant with high atomic mass, and beam neutralization using a cathode or a similar device. In spite of the novel discoveries, Shepherd and Cleaver reluctantly concluded that the ion rocket was impractical due to its massive power requirements. Various scientists focused on the practicality of this technology

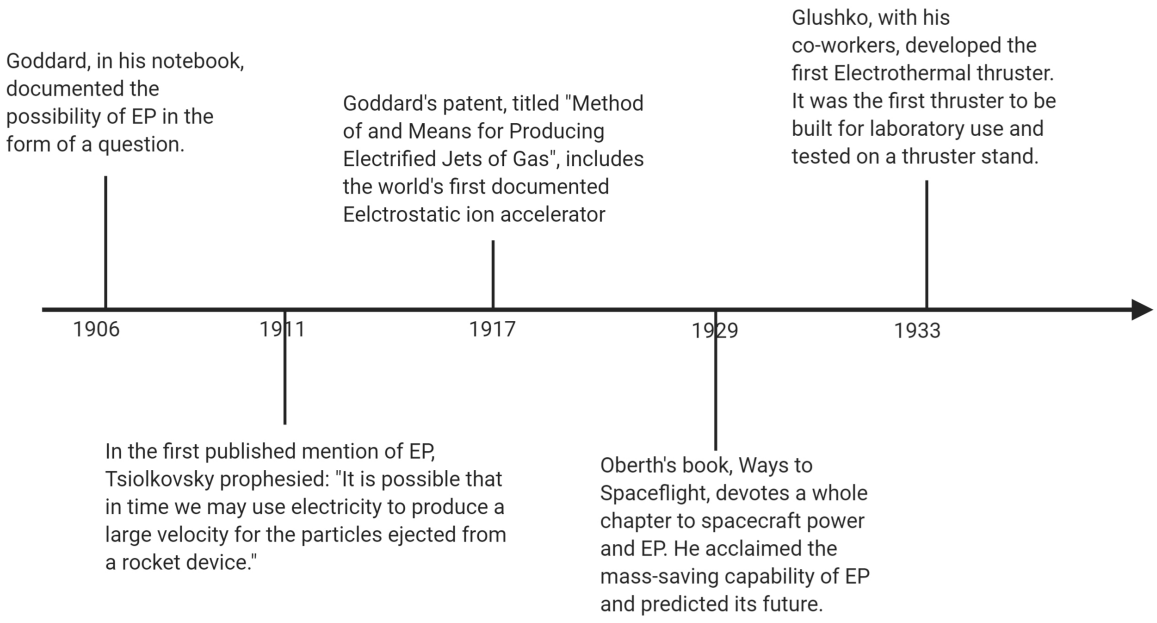

Figure 2.1: Timeline of developments in EP technology from 1906 to 1933.

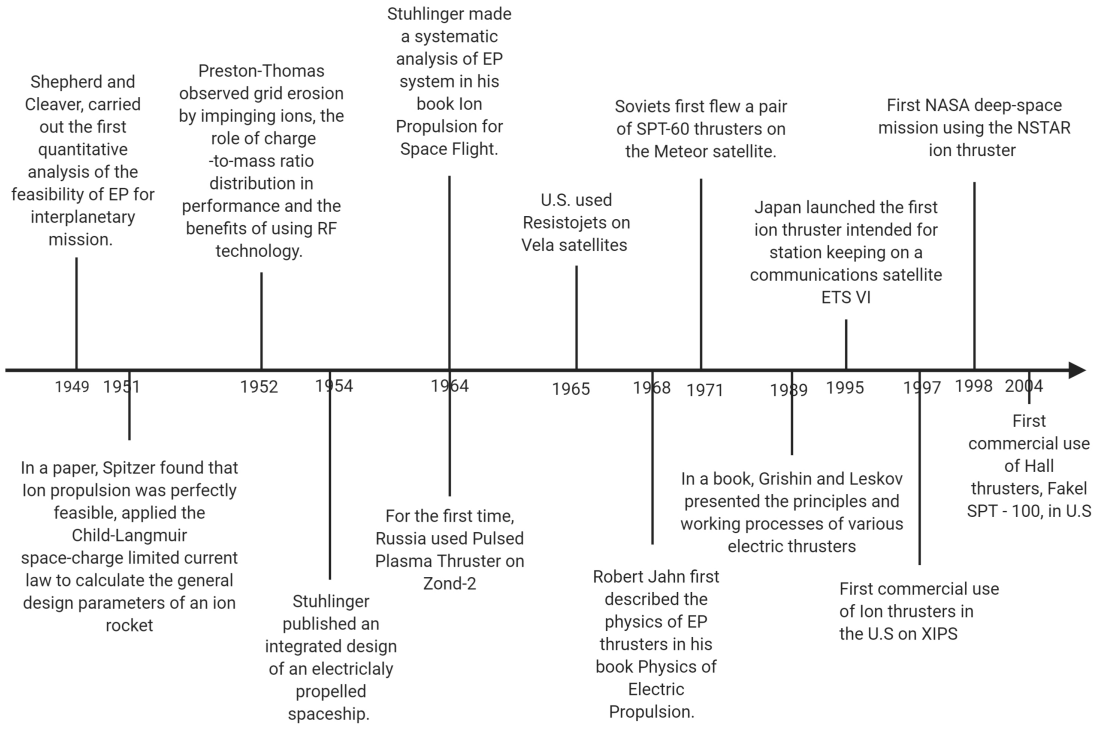

Figure 2.2: Timeline of developments in EP technology from 1949 to 2004.

instead of the physics driving these devices. This was due to the infancy of astronautics and the conceptualization of EP as the domain of human-driven interplanetary vehicle.

The launch of Sputnik in 1957 allowed the world to foresee the value of near-earth commercial satellites and the role of EP systems. EP research programs were established in the U.S., Russia, Japan, and Europe to develop the technology and deem it flight proven. The simplicity and ease of operation of an EP system led to its adoption by the commercial sector. Over the following years, the commercialization of the space industry and the increase in the demand for communication satellites has led to the advancement of EP technology. Recently, the application of EP has widened from GEO satellites to LEO satellites and is gradually moving towards deep space missions to asteroids, moons and other planets in the solar system. Staying true to its initial inspiration, it is certain that EP systems will play an integral role in the future of spaceflight and human exploration.

2.1 Electrostatic thrusters

Ion gridded thrusters and Hall-effect thrusters are commonly used electrostatic EP devices. Figures 2.3 and 2.4 show schematic diagrams of a Hall-effect thruster and ion gridded thruster, respectively. Both of these devices generate plasma by establishing an electric field between an anode and a hollow cathode device. The anode doubles as a discharge chamber wall in ion gridded thrusters, and as a gas distributor in Hall-effect thrusters. The hollow cathode plume acts as an electron source, ionizing the injected gas and neutralizing the ion beam. The thrust produced can be described as [1],

$$T = \gamma \dot{m}_i v_i = \gamma \sqrt{\frac{2m_i}{e}} I_b \sqrt{V_b}. \tag{2.2}$$

Based on this, the measure of thrust efficiency or the specific impulse can be written as [1],

$$Isp = \frac{\gamma \eta_m}{g} \sqrt{\frac{2eV_b}{M}}. \tag{2.3}$$

In a Hall thruster, the electrons from the hollow cathode are drawn into the dielectric channel using an electric field and a radial magnetic field prevents them from flowing towards the anode. This E x B drift traps the electrons, causing them to spiral along the magnetic field and ionize the propellant atoms. The axial electric field then accelerates these ions along the discharge chamber to produce a thrust beam. Magnetic shielding is employed to protect the dielectric walls from sputtering, thereby increasing the thruster life. Similarly gridded ion thrusters use magnetic confinement to minimize electron losses to the anode wall. In these thrusters, ions from the discharge chamber plasma flow towards the biased grids. Multiple intricate grids are used to accelerate the plasma

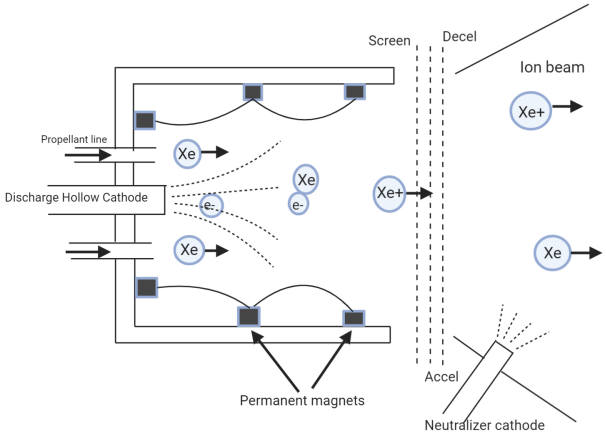

Figure 2.3: Ion thruster schematic

to produce an ion thrust beam. Due to acceleration of ions using grids, the discharge current is space-charge-limited. The maximum current density is given as [1]

$$J_{max} = \frac{4\varepsilon_0}{9}\sqrt{\frac{2e}{m_i}}\frac{V^{\frac{3}{2}}}{d^2}. \tag{2.4}$$

Table 2.1 summarizes the main characteristics that differ for Hall and ion thrusters. Hall thrusters are simple in design but involve much more complicated physics compared to ion gridded thrusters [8]. Acceleration of electrons in a quasi-neutral plasma eliminates the space charge and allows a maximum ion current to be extracted, which is given as [8]

$$I_{max} = A_g J_{max}. \tag{2.5}$$

On the other hand, in ion gridded thrusters this maximum ion current is space-charge-limited. The remarkable capability of Hall-effect thrusters to generate and maintain a large electric field, by decreasing electron movement using a radial magnetic field along with the ionized neutral atoms, allows them to produce comparatively higher thrust at a given power. It is important to note that gridded ion thrusters have comparatively higher efficiency and specific impulse. Appendix A describes preliminary design of a low power cylindrical Hall thruster.

The thrust plume in both these thrusters contains various contaminants including ions which can cause serious harm to the spacecraft body by changing its optical and thermal surface properties. Hollow cathode devices are used neutralize this ion thrust beam as well as to supply the

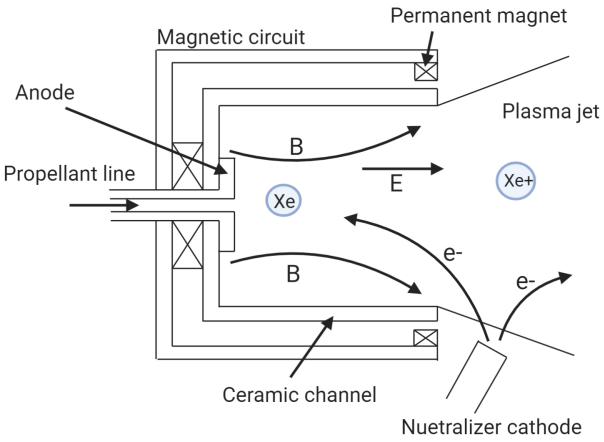

Figure 2.4: Cylindrical Hall thruster schematic

Parameter	Hall thruster	Ion thruster
Specific Impulse (s)	1500-2000	2500-3600
Input power (kW)	1.5-4.5	0.4-4.3
Efficiency range(%)	35-60	40-80
Secondary anode function	Gas distributor	Discharge chamber wall
Ion extraction and acceleration technique	E X B field	Multiple biased grids

Table 2.1: Comparison of typical characteristics for Hall and ion thrusters [1]

electron discharge for ionization of the propellant. The following sections discuss the design and working of a hollow cathode device.

2.2 Hollow Cathode

Early ion thrusters used directly heated tungsten filaments as the electron source. Due to tungsten's high work function, these filaments required operating temperatures of over 2600 K to achieve thermionic electron emission [1]. High temperature operation required a significant portion of the thruster power, reducing its efficiency. Additionally, the filament life was limited to several tens of hours due to rapid evaporation of the filament material at such high temperatures [9]. These

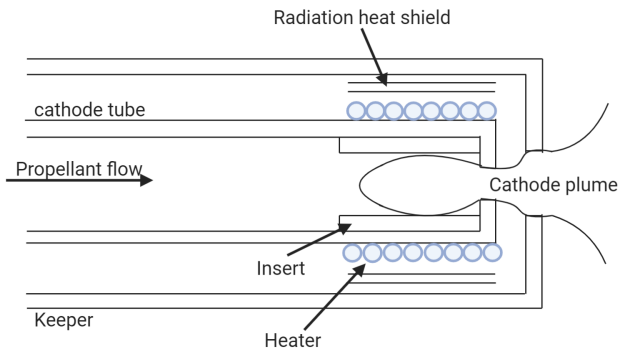

Figure 2.5: Conventional hollow cathode schematic

undesirable features proved this type of cathode to be inadequate for long-life space applications.

Hollow cathodes offer various advantages over a heated tungsten filament and a significantly longer lifetime. The conventional cathode structure (see Figure 2.5) comprises a long hollow refractory metal tube, usually tantalum, with an orifice plate on the downstream end. The diameter of this orifice plate is a few tenths to one millimeter and depends on the desired emission current density. An active electron emitter is placed inside this tube and pushed against the orifice plate using a spring or a pusher tube. This emitter can be made of different materials and is either coated or impregnated with chemical compounds of barium or boron to aid electron emission. The use of such compounds lowers the work function, as explained in Section 2.4, thereby reducing the necessary cathode operating temperature. The thermionically emitted electrons from the emitter ionize the neutral propellant atoms to create a plasma discharge, enabling electron extraction. In the experiments discussed in this thesis, electron current is collected by a positively biased anode, placed downstream of the cathode. A hollow cathode also employs a secondary electrode called a keeper. The keeper encloses the cathode tube, protecting it from high-energy ion bombardment and helps in initiating plasma discharge inside the cathode. It is usually made of refractory metals such as tantalum or molybdenum.

Conventionally, a heater is used to raise the emitter temperature to emissive temperature. However, once the discharge is established, it is self-sustaining, and the heater can be turned off. The cathode operates in a self-heating mode where the emitter is heated by plasma bombardment. However, if the discharge current is too low, the emitter temperature will not be maintained, and the plasma will die out. This heater component in conventional hollow cathodes presents certain limitations to the overall cathode performance which has led to the development of a heaterless hollow cathode configuration which offers various advantages as compared to the conventional cathode (see Section 2.7).

Owing to the rapidly growing micro- and nanosatellite market, there has been a global effort to develop miniaturized EP systems wherein hollow cathodes operate at discharge current less than 1 A. Valuable research [10], [11], [12], [13] has been carried out on hollow cathodes operating at low-current levels with a focus on development of 0-D and 1-D models to predict the cathode operating envelope, study the physics in the orifice region and the effects of orifice geometry on cathode operation with a more recent model [13] for designing thermionic hollow cathodes. One major setback in the development of low-current hollow cathodes is the ability to maintain thermally stable cathode operation in the presence of low plasma heat flux under low discharge current [14]. This demands minimum wall thickness of the cathode tube, which is difficult due to manufacturing limitations and structural strength required to resist the launch loads. Additionally, adequate length of the cathode tube is desired to reduce conduction and keep the emitter region sufficiently warm. Breakthroughs may be possible with the use of low thermal conductivity material, and advanced and/or additive manufacturing, along with detailed research to study the performance of different emitter materials, propellants and orifice sizes at low current. The author of this work aims to contribute to the literature and have a better understanding of the above mentioned aspects of low-current hollow cathode operation without a heater.

2.3 Physical processes in a hollow cathode

Figure 2.6 shows the various plasma regions in a conventional hollow cathode. The gas flow in a hollow cathode device is restricted by the orifice plate to maintain a high neutral density and sufficient pressure to produce a collisional plasma inside the cathode [9]. This is an essential requirement to decelerate the ionized atoms from flowing back and bombarding the emitter surface, causing sputtering and erosion. The electrons are emitted from a narrow strip on the the emitter end facing the plasma [9]. The length over which the plasma inside the cathode is dense enough to support thermionic emission or where the plasma "attaches" is known as the plasma attachment length [15]. Section 2.4 explains the thermionic emission process in detail. Following the ionization of propellant atoms, plasma is formed inside the hollow cathode and a plasma sheath is developed between the emitter surface and the plasma. The electrons emitted from the emitter surface are accelerated across this plasma sheath. Irving Langmuir, in a paper published in 1929 [16], explained that a significant rise in the electron current neutralizes the positive space charge close to the emitter surface. Eventually, the current is limited by space charge, inhibiting the electron current from rising further. The emitter surface is then covered by a double sheath and the ratio of

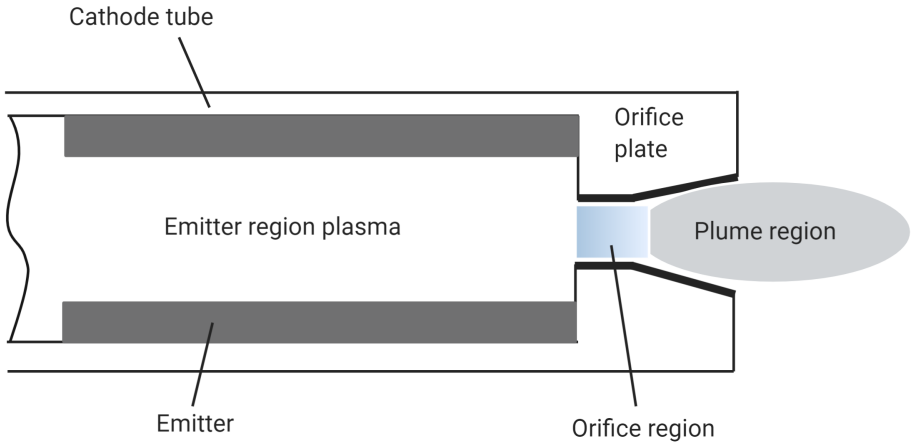

Figure 2.6: The three regions in a conventional hollow cathode

electron current to ion current is given as [16],

$$\frac{I_e}{I_i} = \sqrt{\frac{m_i}{m_e}}. \tag{2.6}$$

If the ion current remains constant, even a change in ignition voltage does not cause a change in electron current and a constant cathode voltage drop is maintained. The high plasma density and the voltage drop across the plasma sheath produce a strong electric field inside the cathode [9]. The emitter surface temperature is increased to the required emission temperature by collision with electrons in the plasma. The emitter surface temperature is dependent on the plasma properties in the emitter region and the cathode emission current. According to the law of conservation of energy, the thermal losses from the emitter surface are balanced by the ion influx [9]. The balance equation is given as [1]:

$$I_t \phi_s + R{I_d}^2 = I_i U^+ + \frac{5}{2} T_{eV} I_e + (2T_{eV} + \phi_s) I_r e^{-\phi_s / T_{eV}}. \tag{2.7}$$

Here, I_t is the thermionic electron current, ϕ_s is the voltage across the sheath on the cathode surface, R is the plasma resistance, I_e is the discharge current, I_i is the ion current generated in the emitter region, U^+ is the propellant ionization potential and I_r is the electron flux due to random electrons at the sheath [1]. Owing to the absorption of radiated energy by the dense optically thick plasma, Equation 2.7 ignores the excitation and radiation losses.

Further, this internal plasma couples the emission current to the main discharge plume and the anode plate via the keeper electrode. The main discharge plume consists of electrons, ionized atoms and expanding neutral gas[1]. The appearance of this plume changes as the propellant flow

rate and discharge voltage change causing the cathode to operate in varying discharge modes. Section 2.5 discusses the cathode discharge modes in detail.

2.4 Thermionic emission

The Richardson-Dushman equation for thermionic emission describes the current density as [17],

$$J = AT^2 e^{-e\phi_{wf}/kT}, \tag{2.8}$$

where A = 120 A/cm^2K^2, theoretically. Experiments have revealed that thermal expansion causes the value of A to vary considerably from the theoretical value for different emitter materials due to varied crystal structures, surface coverage and surface density [1]. A temperature correction factor for the work function was introduced by Kohl [18],

$$\phi_{wf} = \phi_0 + \propto T. \tag{2.9}$$

Therefore, Equation 2.5 can be written as,

$$J = Ae^{-e\propto/k}\, T^2\, e^{-e\phi_0/kT} = DT^2\, e^{-e\phi_0/kT}, \tag{2.10}$$

where D is a material-specific modification to the thermionic emission equation. Section 2.2 discussed the development of a strong electric field at the emitter surface. Schottky [19] determined that in the presence of this electric field, electrons in the emitter conduction band are required to overcome a reduced potential barrier, which effectively results in a reduced work function. Consequently, the emission current density is affected and is called the Schottky effect or field enhanced thermionic process. It is included in the emission equation as follows [1]

$$J = DT^2\, exp\left(\frac{-e\phi_0}{kT}\right)\, exp\left[\left(\frac{e}{kT}\right)\left(\frac{eE}{4\pi\varepsilon_0}\right)\right]. \tag{2.11}$$

From the above equations, it is clear that the value of the work function plays a significant role in the hollow cathode performance. Work function is an important surface property of any material and can be described as the minimum energy required to remove an electron from the emitter surface to a point in the vacuum outside the emitter surface. The emitter material selection depends on the material's work function, such that the required operating temperature for a given emission current is low. Since the development of EP, three types of emitter materials were in use [20]: 1) clean metals 2) metals with contaminated surfaces, and 3) nonmetallic electron emitters.

Type (1) constitutes refractory metals such as molybdenum, tantalum, and tungsten, which are known to have work functions above 4 eV. They require extremely high temperatures to operate and

achieve significant emission current density. Elements like cesium, barium, cerium, or thorium, which have good emission efficiencies and high evaporation rate are deposited on a refractory base metal to reduce the work function and are classified as type (2) emitters. This type of emitter has a limited application due to the evaporation or sputtering of the deposited layer due to ion bombardment. Type (3) emitters are most efficient but cannot be operated at high current densities since they are prone to excessive evaporation [20].

In 1955, Levi [21] suggested the use of dispenser cathode. In a dispenser cathode, oxide material reservoirs are fabricated into tungsten, such that the emitter is continuously supplied with an oxide layer to lower the work function. Different molar constituents of barium, calcium oxides and alumina are used to obtain the desired current density. Although these cathodes have low work functions under about 2 eV [1], impurities in the propellant or the propellant feed system can lead to erratic emission behavior and shorter lifetime.

LaB_6 is a refractory ceramic electron emitter material which has been in use since 1971 in Russian Hall thrusters [1]. In 1951, Lafferty [20] discovered its application in hollow cathode devices. This reddish-purple compound has a cubic crystal structure and the strong binding forces between the boron atoms account for its refractory behavior with melting point of 2210°C. Sufficient temperature causes evaporation of metal on the LaB_6 emitter surface which is replaced by diffused atoms from the lower surface layer, keeping the evaporation losses minimum and constantly maintaining an active cathode surface. Figure 2.7 plots the emitter evaporation rate versus the emission current density for commonly used emitter materials. LaB_6 emitter provides high performance when compared to a dispenser cathode, due to slightly higher work function of 2.67 eV.

In a LaB_6 emitter, the bulk material is thermionically emissive and is responsible for establishing the work function unlike the dispenser cathodes where chemistry of the different constituents is directly involved in establishing the work function. Therefore, a LaB_6 emitter can withstand propellant impurity levels two orders of magnitude higher than dispenser cathode and to an extent is unaffected by impurities including atmospheric oxygen. Additionally, LaB_6 emitters do not require any significant conditioning and can be activated by heating it to high temperatures, unlike dispenser cathodes that require activation procedures.

Despite the insensitive behavior of LaB_6 at higher partial pressures, several studies have revealed the poisoning of dispenser cathodes [22] and LaB_6 cathodes [23] due to oxygen, water, CO_2, and air. The magnitude of change in the emitter characteristics depends on the type and quantity of the gas adsorbed, extent of interaction between the gas and the emitter surface and the emitter temperature. Gallagher [23] experimentally showed that the gas-poisoning pressures for a LaB_6 emitter are a few orders-of-magnitude higher than that for the other emitter materials. He

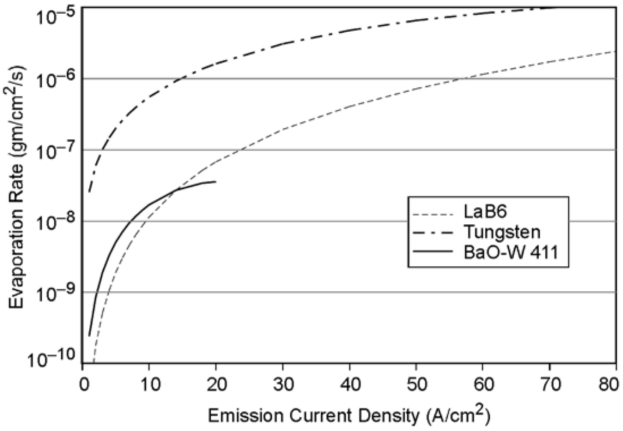

Figure 2.7: Evaporation rate of commonly used emitter materials [1]

also showed that the aversion of a LaB_6 emitter to contamination is equivalent to that of tungsten.

The research presented herein uses a LaB_6 emitter for its cathode design. Previous VTHHC research [2] reported significant poisoning of the LaB_6 emitter over the various testing phases. Visual observation, using an optical microscope, revealed that both the faces of the emitter were significantly covered with lanthanum oxide La_2O_3 with some exposed LaB_6. It was hypothesized that the oxygen present in the flow system must have been beyond the poisoning limits [23] for a LaB_6 cathode. It was also observed that the graphite tube supporting the emitter led to graphite deposition on the emitter surface due to rapid, repeated and unstable arc formation and dissipation. Improvement in the experimental setup to ensure a leak-proof propellant system resulted in a less significant La_2O_3 deposit on the emitter surface.

2.5 Different modes of hollow cathode discharge

Decades of hollow cathode research shows that the discharge plume exhibits distinct behavior under different operating conditions. Rawlin and Pawlik [24], and Csiky [25] were the first to qualitatively observe and identify these operation modes as “spot” and “plume” mode for a mercury cathode. The former is characterized at a high current and low voltage with a bright spot just downstream of the keeper orifice extending only a few millimeters, while the latter is a visible luminous plume extending in a cone, several centimeters from the keeper orifice plate at low current and higher voltage. When in plume mode, an appreciable level of noise, due to oscillations in keeper voltage, is observed which consequently leads to keeper erosion, thereby limiting cathode life. Extensive theoretical and experimental studies [26], [27], [11] have been carried out to study the physics behind the two modes and conditions required to operate in the favorable spot mode.

To operate the hollow cathode in spot mode, it is important to understand the transition between these modes. In this section, the author aims to provide a brief summary of the main findings. Several transition criteria have been proposed, but the researchers have not reached a consensus on the physics underlying the transition process and the plume mode operation. In general, the transition takes place when $I_d/\dot{m}$ is greater than a constant dependent on the magnetic field employed in the thruster and the hollow cathode geometry. Potrivitu [12] showed that this criterion is not applicable to hollow cathodes operating at discharge currents lower than 1 A.

Csiky [25] suggested that the ionization process in the orifice region is the governing process to understand mode transition. Investigations carried out by Fearn and Philip [28] to study the effect of orifice geometry on transition point agree with the suggestions provided by Csiky. Furthermore, they hypothesized that in the plume mode the plasma attaches to the orifice plate only, and that the transition to spot mode occurs when the plasma attaches itself to the emitter due to increased current. Mandel and Katz [11] postulated that the collection of discharge current by the sheath around the keeper plays an integral role in the discharge mode transition process, also citing orifice processes as the key to mode determination. More recent studies [29], [26], [27] show that the plume mode is governed by ionization oscillation and ion acoustic turbulence. In 2005, Goebel [30] showed that the discharge transition is affected by the anode distance and the anode design, modifying the plasma generation rate and density in the plume region. Moreover, ionization frequencies in the discharge plume were found to be comparable to the measured oscillations in the plasma [30]. This establishes the claim that the plume mode is associated with the propellant ionization process and the plasma oscillations. Plume mode operation burns out more propellant causing the discharge to extinguish with the propellant flow [1]. These instabilities can be prevented by selecting appropriate propellant flow [30] to modify the rate of ion production. Additionally, Goebel [31] suggested injection of neutral gas in the plume region to improve the keeper lifetime.

Csiky [25] observed that high flow rates and short anode distances were associated with the spot mode. His calculations for the mean free path in the orifice channel establish that the spot mode is characterized by high plasma density in the discharge region and a lower electrical resistance of discharge. From his calculations for the flow density of fast electrons, it is evident that to operate in the spot mode it is necessary for the equipotential sheath edge to be formed deep enough in the cathode so that most electrons leaving the sheath are trapped in the orifice region. A spot-like bright structure is observed during spot mode operation because only the propellant atoms near the cathode tip are ionized and excited by the fast electrons while the rest of the cathode-anode gap appears dark [12]. Contrary to the observations made for the spot mode, low flow rates and

larger cathode-anode distances result in plume mode. The sheath edge in plume mode spans the orifice [25], [32] and a potential gradient is observed in the plume region only. The inability to produce desired discharge current due to low plasma density causes the keeper voltage to rise and become unstable. Probe measurements by Goebel [31] showed that these voltage oscillations were associated with the propellant ionization in the plume mode. Table 2.2 summarizes and compares the properties of spot and plume mode.

Spot mode	Plume mode
characterized by high current at low voltage [24], [25]	characterized by low current at higher voltage [24], [25]
appears as a bright spot extending only a few millimeters [24], [25]	appears as a luminous cone-shaped plume extending several centimeters [24], [25]
quiet keeper voltage oscillations observed	noisy keeper voltage oscillations observed
occurs when plasma attaches to the emitter [28]	occurs when plasma attaches to the orifice plate [28]
occurs at high propellant flow rates and short cathode-anode distances [25]	occurs at lower flow rates and longer cathode-anode distances [25]
plasma density is high [25]	lower plasma density [25]
equipotential sheath edge is formed deep inside the cathode [25]	equipotential sheath edge spans the orifice only [25]

Table 2.2: Comparison of characteristics and properties of spot and plume mode

Nikrant [2] noticed a disagreement in the definition of plume mode in the literature. He argued that two distinct plume modes exist, both referred to as plume mode in the literature, one at low discharge currents [28], [24], [25] and one at higher discharge currents [26], [29], [33], [34]. This is because the EP systems are designed to operate in a certain current regime ranging from a tenth of an amp to several amps, or on the order of several tens of amps and therefore, it is unlikely for a study to span the full range of low current and high current plumes. The discharge in high current plume (HCP) and low current plume (LCP) is characterized by unstable oscillation in keeper potential but the reported underlying physics varies, even with regards to the same mode [28], [26], [25], [33], [34]. During previous VTHHC testing [2], the transition process from LCP to spot mode was observed. The cathode body showed signs of plasma attachment to the cathode tube face during the plume mode and expansion of plasma attachment area to the emitter during the spot mode, supporting the proposition of Fearn and Philip [28]. It was also observed that higher

flow rates were required to operate in spot mode at an anode distance of 5 mm from the orifice. Interestingly, sudden reduction in anode voltage oscillations always occurred at 2 A, irrespective of the propellant flow rate, but no change was observed in the appearance of the plume. Instead, a gradual change in current caused the plume appearance to change from spotlike to plume. The author suggests that since most of the VTHHC characterization took place in the plume mode, excessive keeper orifice erosion led to high voltage oscillation plume mode setting in as the current was increased. This mode was assumed to correspond to the HCP mode. Fast Fourier transform analysis of the data suggests the presence of some higher frequency resonant behavior internal to the cathode that does not couple to the plasma, concurring with the finding of Domonokos [10]. The motivation for this work is to investigate the VTHHC operation with krypton as propellant and contribute to the literature on transition of plume mode to spot mode in low power hollow cathodes.

2.6 Propellants

An electrostatic thruster assembly uses the same propellant for both the thruster and the hollow cathode device, conserving the propellant storage tank mass and increasing the thruster efficiency. In an electrostatic thruster, most of the available power is used for ionization of the propellant atoms. Thus, an element which ionizes readily and has a high mass to ionization energy ratio is a desirable propellant. For singly charged ions, this is given by the thruster mass utilization efficiency [1]

$$\eta_m = \frac{\dot{m}_{ip}}{\dot{m}_p} = \frac{I_b}{e}\frac{M}{\dot{m}_p}. \tag{2.12}$$

Section 2.1 shows that the thrust and the specific impulse of an electrostatic thruster depend on the mass utilization efficiency of the propellant. Therefore, it is important to convert a large fraction of the propellant mass into ions and accelerate them to produce thrust. Additionally, the type of propellant governs the extent of thruster wall erosion and the contamination of the spacecraft body and the various optical and digital instrumentation on board. An ideal propellant minimizes these drawbacks, allowing the thruster to operate for longer lifetimes. This demands a propellant with large mass, low ionization energy and chemically inert behavior and of course, ease of availability at low cost.

The first electrostatic thrusters were fueled by xenon, which is heavy, easy to ionize, and chemically inert allowing ease of storage at a high density. Since then, many other propellant options, such as mercury, bismuth, iodine, argon and krypton have emerged. Table 2.3 contains properties of these propellants. Mercury has been investigated and abandoned due to its toxic and hazardous

Element	Kr	I	Xe	Ar	Bi
Atomic mass (amu)	83.8	126.9	131.3	39.9	208.9
First ionization potnetial (eV)	14	10.5	12.1	15.7	7.3
Storage density (gm/cm^3)	0.53	4.9	1.6	1.4	9.8
Melting point (degree Celsius)	-157	113.7	-112	-189	271.4
Boiling point at 10 Pa (degree Celsius)	-208	9	-181	-185	768

Table 2.3: Properties of commonly used propellants [4]

nature, high cost, and its tendency to condense and contaminate the spacecraft components that are above cryogenic temperatures. Iodine and bismuth have high atomic mass and are easy to ionize. Additionally, their capability to be stored at high densities compared to xenon makes them a strong candidate. However, iodine's reactivity and low vapor pressure of bismuth present engineering challenges.

Equation 2.3 shows that the propellant ion mass and the specific impulse are inversely related. Therefore, use of lighter species like argon increases the specific impulse and lowers the cost but the thruster efficiency is negatively affected because of its high ionization energy and small electron-impact ionization cross section. These limitations lead to low thrust performance quality for argon thrusters. Previously, Nikrant [2] has characterized the VTHHC using argon, resulting in some interesting observations that agree with earlier research carried out with argon as propellant [35], [36], [37].

Krypton gas is the most similar to xenon in terms of its ionization properties but it is less expensive. Use of krypton for on-ground development of qualification of EP technologies can reduce the cost and the dependence on the rare noble gas, xenon. Furthermore, krypton is lighter than xenon, resulting in high specific impulse thrusters at the same discharge potential. Detrimentally, the storage density of krypton is low compared to that of xenon, but it does increase dramatically as temperature is reduced. At -50 degree Celsius, stored density of krypton is comparable to xenon at 50 °C [4]. Additionally, krypton is slightly harder to ionize, leading to lower propellant utilization and thruster efficiency because the mean free path for ionizing collisions is relatively large [4]. Studies [4], [38] have shown that the performance penalties associated with the efficiency of a krypton thruster can be minimized by running at high power, flow rate and discharge voltage. The research presented herein uses krypton gas to fuel the VTHHC to study cathode behavior, and to compare it to the research carried out by Nikrant [2] using argon as the propellant.

2.7 Heaterless hollow cathode technology

The heater assembly in a cathode is responsible for raising the emitter surface temperature to the desired thermionic emission temperature. The heater is usually turned off after the arc ignition process. Initially, heaters were essential to the operation of mercury cathodes to prevent condensation before ignition. The replacement of mercury with inert gases has eliminated this requirement. Further, a surge in propellant flow to the cathode during ignition enables heaterless operation of the cathode [39]. Heater failure has been commonly observed and can hinder the hollow cathode lifetime. Hollow cathode heaters are sensitive to fabrication procedures [40]. They usually contain refractory metals and undergo thermal shocks, making them prone to cycling failure [41]. Additionally, the dedicated power supply for the heater leads to increased mass and complexity of the overall system and lower efficiencies due to considerable power consumption. Moreover, the duration of the startup procedure for a conventional cathode is typically hundreds of seconds [42], deeming it unsuitable for microsatellite propulsion and satellite orbit control which requires the hollow cathode ignition to be in the milliseconds time scale. Such missions also require the cathode design to be simple and lightweight.

Thus, to increase the reliability and lifetime of the hollow cathode, several studies [39], [43], [14] have proposed a heaterless hollow cathode (HHC) design. Instead of using external heating, HHCs follow a different ignition process which is discussed in section 2.8 in detail. HHCs have been researched globally for over four decades [14] but have not been employed in space. Despite the mentioned advantages, HHCs pose some challenges [41]. Cold cathode ignition requires high voltage power supplies, increasing the mass of the system. The cathode design is required to allow plasma heating of the emitter to achieve thermionic emission and thermally shield it at the same time. Furthermore, in conventional hollow cathodes, the gradual increase of heater temperature allows conditioning of the cathode surfaces which is not possible in a HHC configuration. Schatz [39] has shown that instant cathode startup results in fast cathode degradation due to severe emitter damage and arc attachment to the emitter's surface.

Interest in HHCs is steadily increasing, and the technology is becoming more mature. It seems likely that some of these systems will soon be flight tested, and if these tests are successful HHCs may become more common in small satellite systems. A recent paper [41] includes a description of all the cathodes that have been developed at various laboratories and universities. This work aims at contributing to the study of HHC devices, their behavior with different propellants and contribute to solving the challenges that remain to be solved.

2.8 Phases of heaterless hollow cathode operation

HHC ignition is split into the following main stages: breakdown, heating, and keeping [44], where nominal operation can be defined as the fully operational state with discharge current flowing between the emitter and anode. It is important for the cathode to go through all three stages in the above-mentioned order for successful ignition.

The breakdown stage commences through a rapid avalanche of ionization, initiating from the cathode tube. This occurs when the neutral propellant atoms are ionized by a sufficiently high voltage, given by Paschen's law which states that, for a given gas, the breakdown voltage is proportional to the product of the static pressure (P) and gap between the electrodes (D) [45]. The breakdown voltage minimizes for an optimum value of P*D called the Paschen minimum. Interestingly, the hollow cathode geometry follows neither of the criteria because the geometry is non-planar, and the pressure is non-static between the two electrodes. Even so, previous research [44], [39] has shown that the trends remain the same. In order to design an efficient hollow cathode, it is suitable to have the minimum breakdown voltage between 200 to 400 V [39]. According to Paschen's law, the breakdown voltage for a HHC may be decreased by lengthening the cathode orifice plate and keeper gap or increasing pressure through flow rate. Several researchers [39], [46], [43] have observed that, in HHCs, gas breakdown may occur at voltages lower than the Paschen minimum and at lower values of P*D. This has been demonstrated by Eichhorn [47] who concluded that due to the axis-symmetric geometry of the cathode, high energy electrons bounce between the hollow cathode electrode walls, enhancing the ionization avalanche effect. Daykin [43] characterized the breakdown voltage variation with changes in cathode to keeper orifice distance and propellant flow rate. He also showed that the effect of keeper orifice geometry is significant than the cathode geometry. With regard to the stochastic nature of the HHC breakdown, most researchers use electrode spacing of several millimeters and pre-ignition pressure values of the order of tens of torr to achieve efficient breakdown. Breakdown is characterized by a sharp reduction in the keeper potential and a sharp increase in the current.

The propellant breakdown is followed by a transition phase wherein the temperature of the electron emitter is increased to its operational temperature. In a conventional cathode, this is done using an external heater, unlike the heaterless cathode configuration. During this phase, plasma discharge is maintained between the emitter and the keeper. There are two main types of discharges possible - glow discharge or an electric arc. Glow discharge is characterized by current of few milliamperes at hundreds of volts, where a slight rise in current increases the size of the plasma discharge-electrode interaction region. Cathode heating via glow discharge generation can take tens of seconds. On the other hand, an electric arc is characterized by current of several tens

of amperes at tens of volts. The plasma discharge in the arc regime is localized on a small portion of the electrode heated up to its operating temperature. An electric arc between the emitter and the keeper ensures quick ignition and quick heating of the cathode region where electrical arc attaches. However, if the emitter is still cold, arcing to the cathode structure or to the emitter is observed which consequently causes the cathode structure to deteriorate. Lev [14] reports that cathodes with LaB_6 emitters have a longer heating duration than other emitter materials due to the higher work function of LaB_6. The end of the heating phase is characterized by a thermionically active emitter which supplies the required discharge current through a relatively large area.

The main discharge between the electrodes is established. Now, the cathode operates under a steady state and is self-sustained through sufficient emitter heating. This phase is referred to as the keeping phase and is characterized by current of hundreds of milliamperes at tens of volts.

Chapter 3

Experimental equipment and procedure

Quantifying the differences in operating characteristics between the heaterless hollow cathode behavior with argon and krypton as propellant has been the key aim of the experimental investigation. The equipment discussed in the following sections is essential to the overall research. Figure 3.1 displays a schematic of the subsystems involved in the VTHHC testing. Over the course of VTHHC developmental efforts, it has been observed that the quality of vacuum and a clean, leak-proof gas feed system play key roles in determining the cathode performance and lifetime. Therefore, utmost care is taken to maintain a clean working environment and to reduce contamination.

The terms downstream and upstream are used in relation to the flow direction of the gas.

3.1 VTHHC design

A first-generation, laboratory model of a LaB_6 heaterless hollow cathode (VTHHC) is characterized in this study. The VTHHC design is simple and modular in construction, enabling easy replacement of any component. This enables visual examination of the cathode's internal surfaces, allowing non-destructive analysis post-experiment. If the cathode fails, only the damaged component can be restored, eliminating the necessity of manufacturing other cathode parts. This design philosophy has allowed constant improvement and re-designing throughout the development process without altering the complete design.

An engineering schematic of the VTHHC is presented in Figure 3.2. The different colors in the figure indicate various materials, where light gray corresponds to 304 stainless steel, dark gray to tantalum, white to boron nitride, yellow to alumina, black to graphite and purple to LaB_6. The overall length of the cathode is 126 mm. A 103 mm long tantalum cathode tube with 5 mm inner diameter and a thickness of 0.8 mm houses the LaB_6 emitter on the downstream end. The

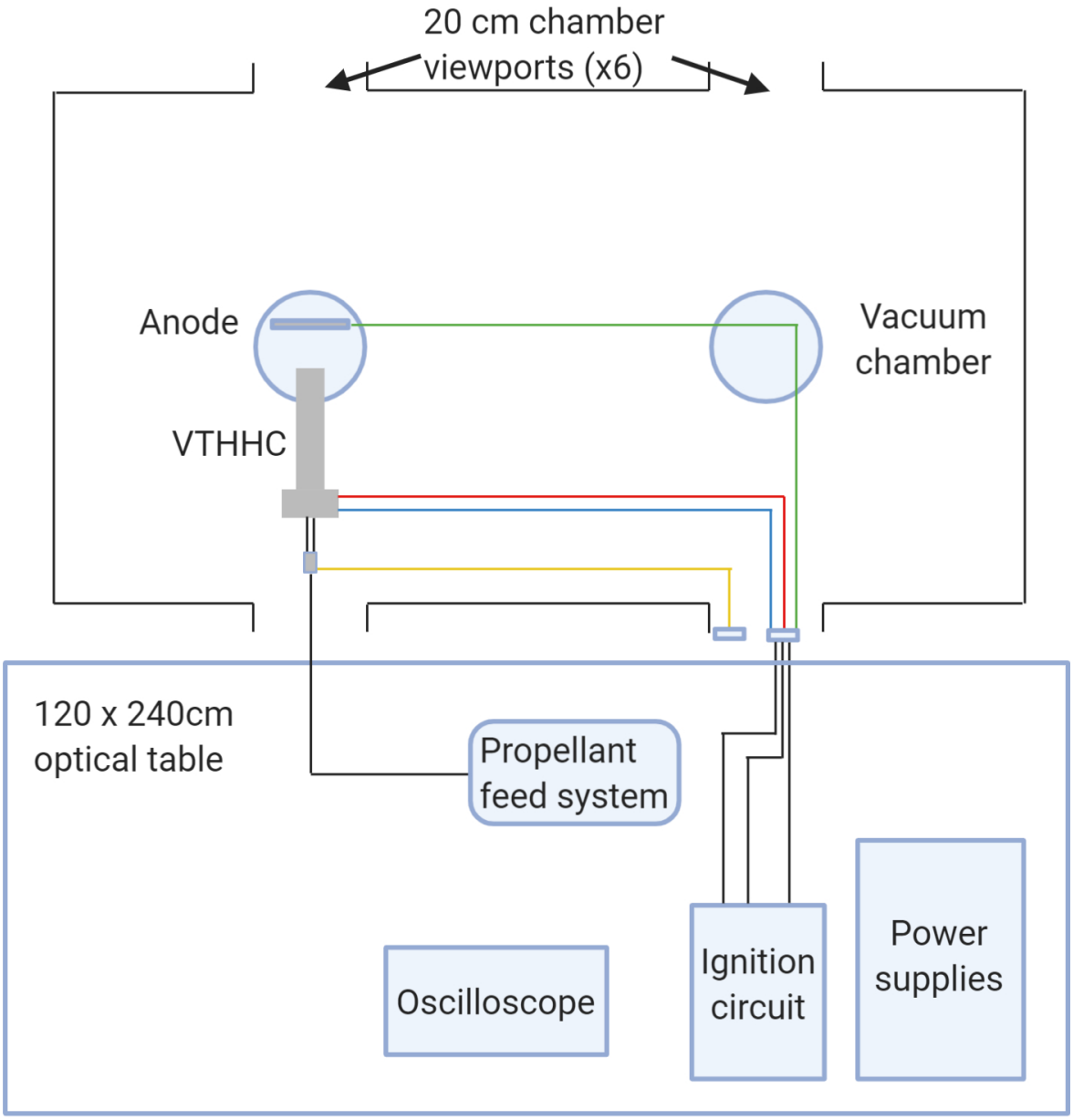

Figure 3.1: Schematic of the VTHHC and its subsystems

emitter is a 10 mm long cylinder with 3.4 mm inner diameter and 0.5 mm thickness. A fine 0.2 mm thick graphite sleeve with a lip at both ends, electronically connects the LaB_6 emitter to the cathode tube while separating it mechanically to inhibit boron diffusion [48]. The graphite sleeve is necessary because the diffused boron can make the cathode tube brittle, leading to structural failure [20]. Although the LaB_6 emitter does not require any dedicated activation procedures, the graphite sleeve must be conditioned before use to reduce the outgassing of CO and CH_4, which can lead to emitter poisoning [23]. The graphite sleeve is baked in a vacuum furnace at 1000 degree Celsius

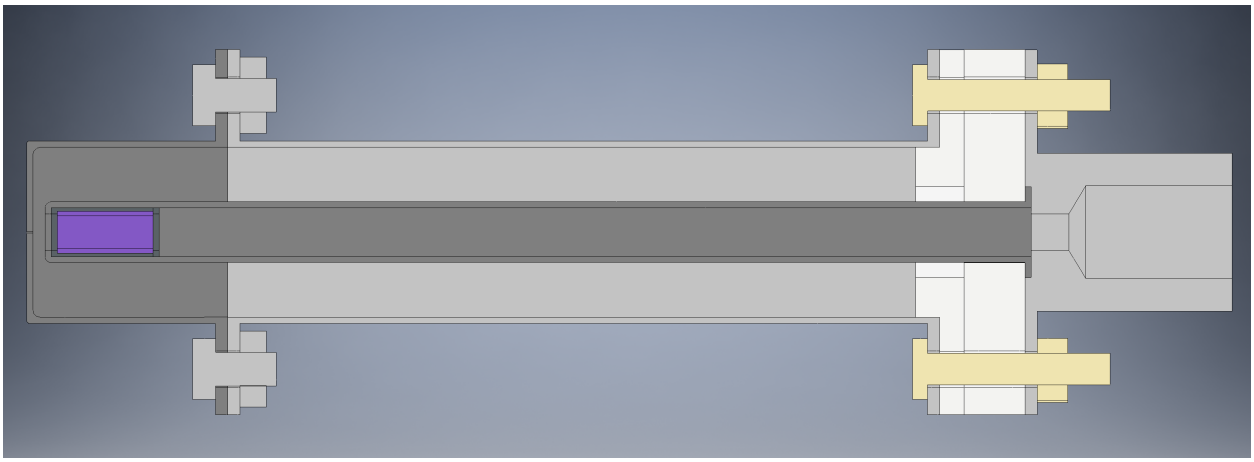

Figure 3.2: Schematic of the VTHHC design [2]

and 10^{-5} torr for two hours [49] at the Advanced Manufacturing Team Characterization Lab at Virginia Tech. The graphite sleeve and emitter assembly is held in place using a tungsten spring (not shown in Figure 3.2) to restrain its movement along the cathode tube length. An enclosed keeper design has been adapted to double as a radiation enclosure for the cathode. The keeper is designed such that one half of it is made of tantalum and the other half is stainless-steel, acting as a support to reduce the material cost and allow easy access to visually inspect the downstream end of the keeper post-testing. Both the tantalum keeper and the stainless-steel support have 17.8 mm inner diameter and 19 mm outer diameter and are held together by flanges, connected using a bolt and nut connection. The keeper orifice diameter and length are 0.2 mm and 0.64 mm, respectively, enabling an adequate internal pressure at low propellant flow rates at degree Celsius [2]. The downstream end of the cathode tube is separated by 1.27 mm from the inner keeper face. Ceramic barrier disc, with a small lip to prevent breakdown encouraged by the sharp internal edge at the keeper base, electrically isolates the keeper and emitter. All the parts are concentrically constrained by design and clamped together with alumina screws for electrical insulation. The VTHHC is a open-end emitter orificed keeper configuration type hollow cathode. This configuration is unique for heaterless hollow cathode devices and yields pressure in the order of tens of torr between the electrodes, enabling initial gas breakdown close to minimum of the Paschen curve.

Nikrant [2], during previous VTHHC testing, discovered that these alumina screws were insufficient to clamp the cathode components together causing the cathode to leak at the base and perform poorly. Two thick stainless-steel sheets along with ceramic screw sleeves and metal screws (not shown in Figure 3.2 are utilized to provide an additional clamping force as well as provide electrical isolation. Tests [2] showed a considerable reduction in the leak at the base. A stainless-steel flange is threaded with 7/16-20 straight threads to mount the VTHHC assembly to a Kf-40

feedthrough which housed a Swagelok 1/4 inch tube. This mounting system includes a dielectric Swagelok fitting to electrically isolate the cathode from the chamber. A thin stainless -steel plate mounted on a polycarbonate base for electrical isolation is used as a planar anode during testing.

3.2 Power subsystem

The VTHHC electrical system is shown in Figure 3.3 . This circuit is responsible for running the cathode during both ignition and steady-state discharge states. A Sorensen XG 600-1.4, 600V, 1.4 A power supply supplies the VTHHC circuit with high voltages at a current limited setting for gas breakdown and emitter heating. This power supply is referred to as the keeper power supply. The diode downstream of the keeper power supply allows the keeper to float without drawing any current during steady-state operation with the keeper supply turned off. The anode voltage and current is regulated by a Sorensen 300-2, 300V, 2A power supply during the steady-state discharge. This power supply is referred to as the anode power supply. Figure 3.3 shows an image of the circuit box designed for the purpose of VTHHC testing. BNC cable connectors are used to connect the circuit box output to a KF-40 power feedthrough, which is mounted on the chamber. Inside the chamber, the output leads of the power feedthrough are connected to the emitter, keeper and anode using PEEK insulated wires via ring terminals.

3.3 Propellant subsystem

Grade 4.5 krypton with a purity of 99.995 % is used for propellant supply to the cathode. A single stage brass regulator set to 30 psig is connected in series with the propellant cylinder, as show in figure 3.4. An Alicat Scientific MC-5-SCCM-D mass flow controller, calibrated for krypton, with a full-scale flow of 50 sccm controls the propellant flow to the hollow cathode. The flow controller has an uncertainty rating of $\pm$ (0.8 % reading + 0.2 % full scale) and can be controlled using the digital display screen. A Swagelok purge valve is installed between the propellant cylinder and mass flow controller to vent propellant line pressure before disassembly, thereby ensuring personnel safety. The mass flow controller is followed by a Swagelok check valve to avoid back flow from the chamber to the propellant cylinder, and a shutoff valve to control the flow to the cathode. The feed system schematic is shown in Figure 3.4. All the components described above are connected using stainless-steel tubing, and fittings with VCR metal gasket seals. This setup minimizes the diffusion of atmospheric air into the system and possibility of trapped volumes within the feed system, which could potentially contaminate the cathode as observed by Nikrant[2]

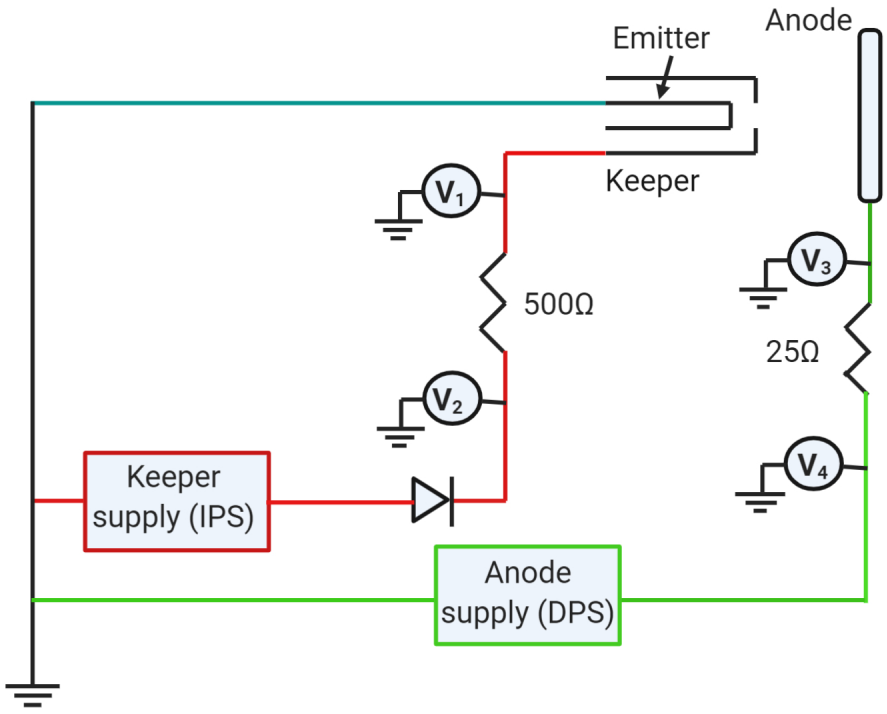

Figure 3.3: VTHHC ignition circuit schematic

during his experiment. Additionally, the valves are chosen to have metal seals and minimal use of polymers or lubricants in their construction.

3.4 Vacuum system

The VTHHC testing is carried out in the vacuum laboratory located at the Center for Space Science and Engineering Research at Virginia Tech. Figure 3.1 shows the chamber with a diameter of 1 m and length of 1.2 m. It is connected to a roughing pump and a cryopump. An auxiliary chamber, attached to the main chamber via a gate valve, houses the cryopump allowing re-pressurization of the main chamber and adjustment of the test setup while the cryopump stays cold. The Trivac D40B roughing pump has the capability to bring down the chamber pressure to 50 militorr over a period of 45 minutes, approximately. The TorrMaster TM500 cryopump takes over thereafter, to bring the pressure to the microtorr range over a period of 4 hours. Cryopumps provide an adequate pumping speed and maintain a pristine environment for cathode exposure. During cathode operation, the chamber pressure is maintained at 1.4 x 10^{-3} torr and is measured by Varian's BA2c senTorr Gauge Controller. Three KF-40 feedthroughs on the chamber are utilized to mount the cathode,

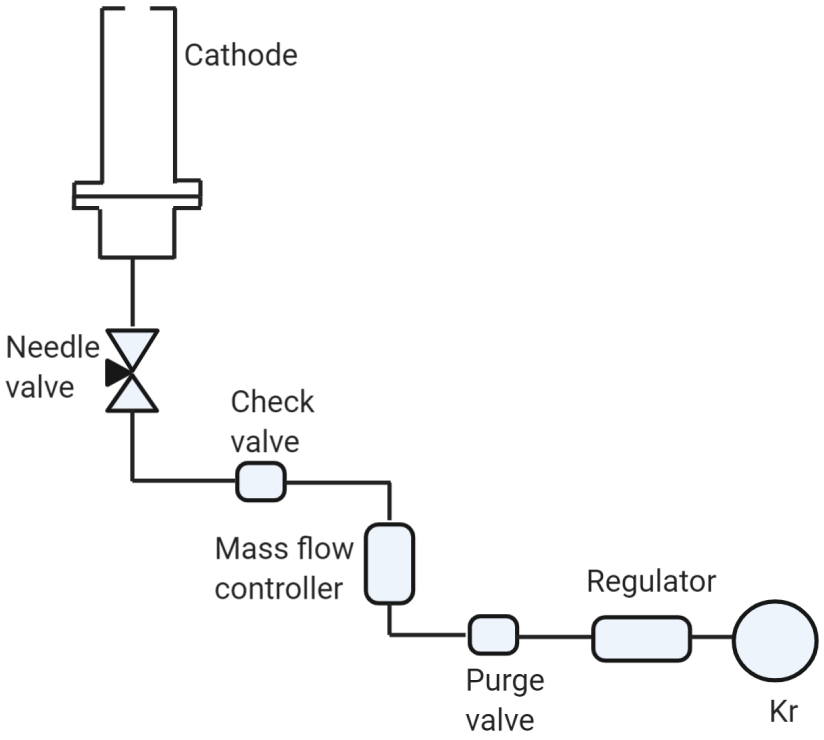

Figure 3.4: VTHHC propellant feed system schematic

supply power and for diagnostics purposes.

3.5 Diagnostics equipment

An Agilent DSO-X-2024A oscilloscope along with 10:1 attenuated passive voltage probes are used to monitor voltage characteristics of the hollow cathode. Figure 3.3 shows the probe locations. V_1 and V_3 represent the emitter-keeper and emitter-anode voltages, respectively. V_2 is measured to calculate the current through the keeper using the voltage drop across the resistor between V_3 and V_1. Similarly, V_4 is measured to calculate the current through the anode. The voltage per division value for the oscilloscope is set to the maximum value of 50 V/div to capture the full range of emitter-keeper voltage during ignition. As a result, the bit depth of data taken during ignition is approximately 2 volts, introducing errors. During steady-state operation the voltage per division value is set to 5 V/div since the voltage does not vary during this state.

An Omega Engineering PX409-005A10V pressure transducer with a range of 0-5 psia is used to measure the internal cathode pressure. The low flow rates and short ($\approx$ 30 cm) distance to the cathode orifice allow the flow losses through the propellant feed tubing to be neglected. An Agilent

DSO-X-1104G oscilloscope measures the output voltage signal from the pressure transducer.

The dielectric separator is responsible for electrically isolating the cathode assembly from the chamber and is temperature limited to a temperature of 93 degree Celsius. To avoid overheating and melting of the dielectric fitting, an Omega Engineeing CO3 series cement-on K-type thermocouple is used to monitor the temperature via a Fluke digital thermometer. A KF-40 thermocouple feedthrough connected the thermometer to the thermocouple, which is located inside the chamber.

A Canon 80 D camera is mounted on the viewport, located on the top left of the vacuum chamber (see Figure 3.1). This optical instrument is used to visually observe the cathode discharge plume and capture the various discharge modes.

Chapter 4

VTHHC experimental investigation

It is the hope of the author that the experiments reported in this chapter establish a basis for understanding the behavior of a low current HHC, and thereby developing a more efficient cathode. Performance data such as breakdown and discharge characteristics at varied discharge currents and cathode-anode distances are collected using krypton gas as the propellant. Voltage across the emitter-keeper gap and the emitter-anode gap is recorded to examine the cathode plume-region plasma. Since the cathode is a first generation laboratory model, a few requirements for flight hardware were either relaxed or omitted.

4.1 Ignition behavior

Based on the experimental observations, the following ignition procedure is carried out to collect relevant data for further analysis:

1. Set flow rate to 0.3-0.5 sccm.
2. Turn on keeper power supply at 400 V with a current limit of 100 mA.
3. Once the breakdown is achieved, increase the flow rate to the desired operating point.
4. Increase the current limit on the keeper power supply to 250 mA.
5. Turn on the anode power supply at 130 V with a current limit of 2 A.
6. Once the discharge forms, leave the keeper power supply on to provide additional heating to the cathode structure.

7. When the discharge characteristics stabilize, turn off the keeper power supply, allowing the keeper to float.

8. Leave the anode power supply on for 10 minutes or more to allow the cathode to approach thermal steady-state.

Section 2.8 shows that the minimum breakdown voltage for krypton, depending on the keeper orifice size and the cathode-keeper distance, is achieved at low flow rates. During experiments, it is found that the required flow rates for stable operation are between 9 and 12 sccm. It is difficult to achieve breakdown at reasonable voltages at flow rates between 9 to 12 sccm. Therefore, a 100 mA glow discharge initiation procedure between the keeper and emitter is carried out at flow rates between 0.3 to 2 sccm. Once the breakdown characteristics are observed, the flow rate is increased to the desired operating flow rate (9 - 12 sccm) with the keeper power supply on, to gradually warm the cathode. The plasma discharge is maintained between the cathode tube and the keeper with the current limited to 250 mA. This is the heating phase discussed in Section 2.8 where the temperature of the emitter is increased from cold to operational temperature. The cathode is observed to enter the arc regime, characterized by voltages of tens of volts and high current, after 2 to 3 minutes of discharge initiation. This allows quick heating of the emitter to which the electric arc attaches.

Because the emitter is still cold immediately after breakdown, an arc can attach to any conductive material at the cathode potential. To avoid arcing and damage to the cathode structure, an electric arc discharge is established only after the emitter surface temperature is increased slightly using a glow discharge. Glow or electric arc discharge is controlled by current-limiting the power supply. This heating process lasts for several minutes, heating up the emitter up to thermionic emission temperature. At this point, transition to main discharge is achieved by turning on the anode power supply. The time required to heat the cathode is observed for various preliminary tests, developing an understanding of cathode operation. Discharge is achieved almost instantly when the anode power supply is turned on. After allowing the main discharge to stabilize for a few minutes, the cathode is operated at a steady state condition with the keeper supply off. Unfortunately, the main discharge dies after lasting for a little over a minute. The discharge plume is observed to grow more luminous during this event. This event may take place due to insufficient power deposition on the emitter, which is required to maintain the emitter surface at the thermionic emission temperature, possibly due to excessive power radiation.

Unsuccessful ignition is observed at flow rates of 6 and 7 sccm when the anode current is set too low. The main discharge lasts for a minute before extinguishing. This process occurred repeatedly for several minutes after which the main discharge shifts to an internal discharge between the cathode tube and the keeper. Similar observations were made by Nikrant [2] during the VTHHC

tests with argon. A band of unfaded tantalum separating two areas of plasma attachment was seen when the cathode was operated with argon [2]. On the basis of this visual observation, Nikrant [2] argued that two different stable internal discharge configurations exist. Interestingly, during the VTHHC tests with krypton, the band of unfaded tantalum is absent and the presence of two different internal discharge configurations is not observed. Instead, after approximately 60 minutes of testing at low current, the downstream end of the cathode starts glowing, indicating that a discharge does exist inside the cathode with the plasma arc attached to the emitter.

Main discharge initiation is attempted at cathode-anode distances of 5, 20 and 35 mm only. The main discharge behavior at cathode-anode distances of 20 and 35 mm is discussed in detail in the following sections. At the cathode-anode distance of 5 mm, although the main discharge is initiated successfully, the tests were aborted only a few minutes after the main discharge initiation due to excessive anode heating (see Section 4.3).

4.2 VTHHC performance characteristics

Experiments are conducted with krypton as propellant for discharge currents ranging from 0.2 A to 1 A at 9 - 11 sccm flow rates and cathode-anode distances of 5, 20, 31 and 35 mm. To study the change in performance with the use of krypton, these results are compared with previous tests carried out with argon for discharge currents between 1 A and 3 A at 12 - 17 sccm flow rates, for a fixed cathode-anode distance of 5mm [2]. The breakdown voltage for the VTHHC is experimentally determined by gradually increasing the keeper supply voltage at flow rates starting from 2 sccm followed by 1, 0.5 and 0.3 sccm. The keeper supply voltage is set to 300 V and gradually increased by 50 V until the breakdown characteristics are observed on the oscilloscope. Voltage is recorded using the voltage probe V_1 (see Figure 3.3) at each breakdown for a particular flow rate and the voltage is re-set to 300 V for a different flow rate before repeating the procedure again. Although this process is carried out numerous times for the different flow rates, only the initial breakdown voltages are plotted. This is done to ensure that the plotted data is recorded at the same cathode condition, unaffected by the cathode temperature after warming up. It is important to note that these excluded data points deviate from the initial breakdown voltage on the order of tens of volts only. The results can be seen in Figure 4.1. The error bars in this figure represent the full envelope of recorded values over a period of 5 ms. The data point for cathode-anode distance of 31 mm at 2 sccm flow rate has a large error associated with it as compared to the other data points. This abnormal behavior can be attributed to a delay in capturing data on the oscilloscope as the cathode appears to have already entered the glow discharge regime.

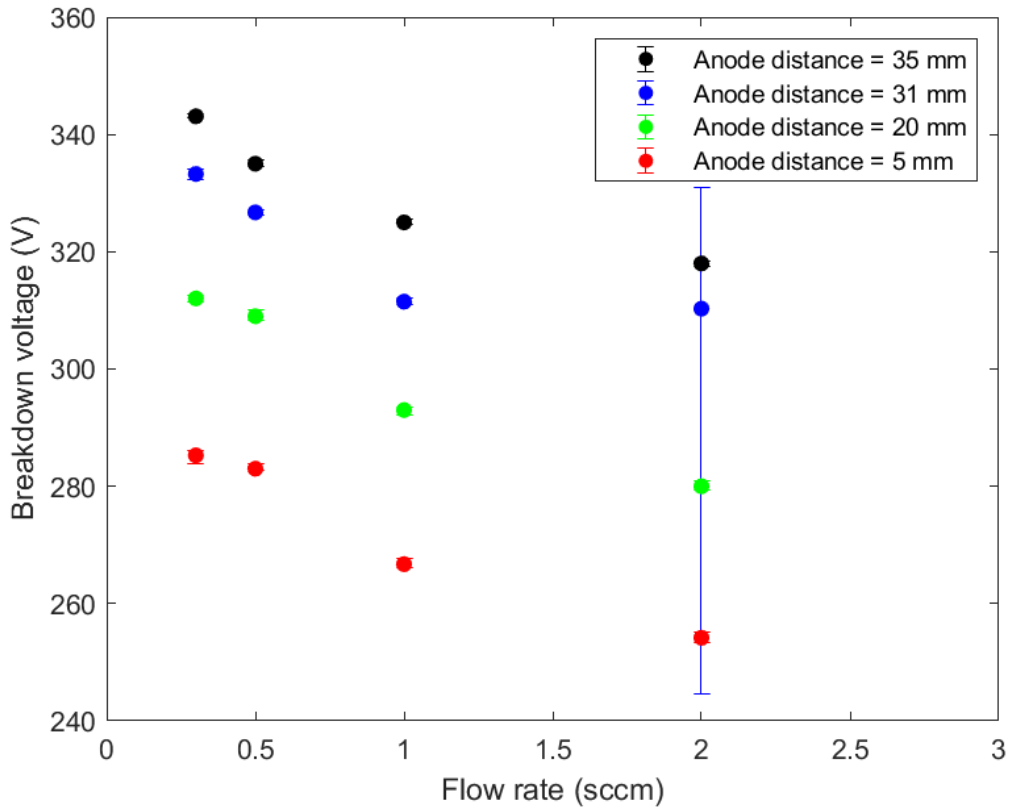

Figure 4.1: Breakdown voltage versus flow rate at varying cathode-anode distances. Error bars show the range of values recorded over 5 ms.

Previous discussion in Section 2.8 explained the dependence of breakdown voltage on the pressure and the gap between the electrodes. With a fixed gap of 1.27 mm, the pressure is varied by controlling the propellant flow rate. As expected from the Paschen curve, the breakdown voltage drops with an increase in propellant flow. The breakdown potential is not impacted dramatically by the flow rate because of the small range of flow rates for which the cathode is tested. Similar results are observed in [43] for a heaterless hollow cathode setup with argon at flow rates between 1 and 30 sccm, showing the dependence of propellant flow rate on the breakdown voltage. During the VTHHC tests with argon [2], the breakdown voltage required to establish the initial ignition glow discharge increased from 350 V to 500 V over the project duration, probably due to deterioration of keeper and emitter surfaces over time. Although this is not observed during the current VTHHC tests, it is interesting to note that the breakdown voltage decreases with the cathode-anode distance. It is difficult to hypothesize the reason for this because the anode power supply is turned off during the initial glow discharge initiation and the breakdown voltage solely depends on the cathode-keeper gap and the keeper geometry [43]. The lower cathode-anode distances are tested during the latter period of the project but the breakdown voltage recorded is lower compared to the higher

distances. Therefore, this behavior cannot be due to the deterioration of emitter and keeper surface conditions over time. Because the breakdown voltage varies over a range of tens of volts only, this behavior can be attributed to delay in capturing the data by pressing the oscilloscope button manually.

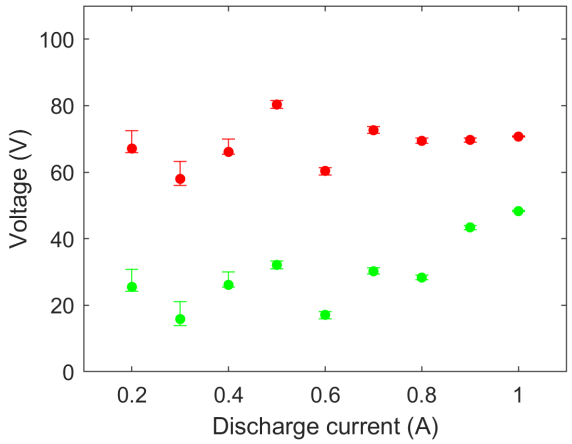

(a) Anode distance = 20 mm, flow rate = 9 sccm

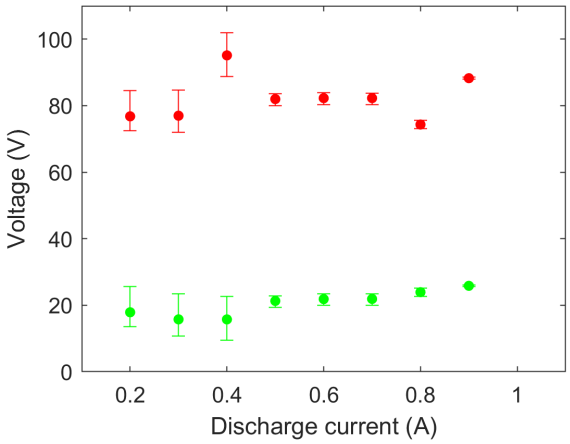

(b) Anode distance = 35 mm, flow rate = 9 sccm

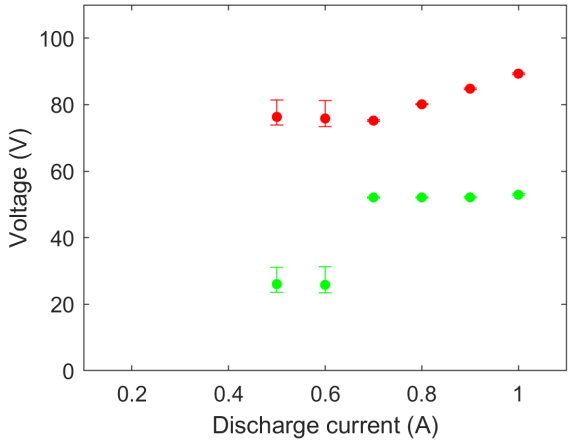

(c) Anode distance = 20 mm, flow rate = 10 sccm

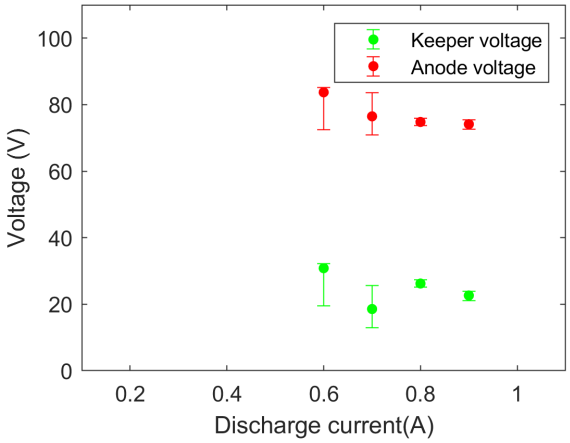

(d) Anode distance = 35 mm, flow rate = 11 sccm

Figure 4.2: Anode and keeper current-voltage characteristics at different anode distance and flow rates. Error bars show the range of values recorded over 5 ms.

The voltage-current characteristics for the VTHHC at different cathode-anode distances are presented in Figure 4.2. Keeper and anode voltage is collected over a period of 5 ms at each discharge current using a voltage probe and an oscilloscope. An average of the data collected over the 5 ms period at a given discharge current represents a data point in Figure 4.2. The voltage-current curves are suggestive of the typical hollow cathode behavior, which exhibits a minimum anode voltage at a certain anode current. This behavior is particular in Figures 4.2a, 4.2b and 4.2c

at discharge currents between 0.6 to 1 A. The drop in anode and keeper voltages may be due to discharge oscillations causing transitions between the spot and plume mode.

Figures 4.2a and 4.2b show that the range of anode voltage increases with an increase in the cathode-anode distance from 20 mm to 35 mm at 9 sccm. This is in agreement with the observations made in [50] for a 25-A class hollow cathode for various cathode-anode distances and anode designs.

The keeper voltage is observed to be lower than the anode voltage and follows the same trend as the anode voltage. For data points at discharge currents over 0.8 A, the keeper voltage does not follow the same trend as the anode voltage hinting at the presence of instabilities inside the cathode which do not couple with the discharge plume (see Section 4.3). Additionally, slightly lower keeper voltages are observed at increased flow rates. This is particularly evident when comparing plot 4.2d, for 11 sccm, with the plots for 9 and 10 sccm, where the keeper voltage shows a difference of $\approx$10 V. Similar voltage-current characteristics were observed in [51]. Comparing these results with the previous VTHHC testing with argon [2], similar anode and keeper voltage trends with the width of the "trough" in anode voltage increasing at higher flow rates are seen. However, the keeper voltage was insensitive to flow rate. Nikrant speculated that this could be due to leakage through the cathode body since the design was susceptible to leaking at the base. Therefore, it is safe to assume that the improved clamp design helped mitigate the leak to some extent.

At low current operation, the discharge extinguished instantly. The cathode successfully operated down to 0.2 A, but eventually extinguished at 0.1 A for the flow rates and cathode-anode distances presented in this work, possibly due to an unsteady thermal state and insufficient heating of the cathode. Nikrant [2] investigated the low flow rate, low current operation at 12 sccm and observed successful cathode operation down to 1 A after which the cathode extinguished at 0.9 A due to insufficient emitter heating.

4.3 Cathode plume behavior

In order to further analyze the deviation of keeper voltage from following the same trend as the anode voltage, discussed in Section 4.2, it is important to decouple the emitter-keeper behavior from the main discharge. The keeper voltage is subtracted from the anode voltage and is plotted against the discharge current, in Figure 4.3. The observed trend is similar to that of anode voltage in Figure 4.2. However, for the higher discharge currents, where the keeper voltage behavior deviates from the anode voltage trend, the data points are somewhat scattered. For Figure 4.3c the data points at higher currents show a linear voltage-current relationship, suggesting a constant

resistivity in the main discharge. Constant resistivity in plasma is a characteristic for spot mode operation in hollow cathodes and coincides well with the results plotted in Figure 4.4.

VTHHC tests with argon [2] showed similar behavior, where the difference in anode and keeper voltage displayed a similar overall trend as the anode voltage aside from a more pronounced voltage increase with an increase in discharge current in the spot mode regions.

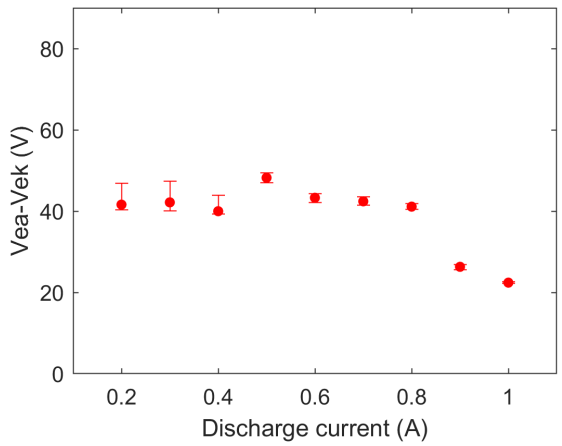

(a) Anode distance = 20 mm, flow rate = 9 sccm

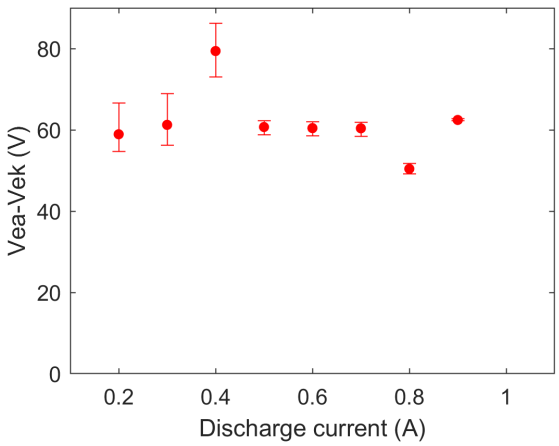

(b) Anode distance = 35 mm, flow rate = 9 sccm

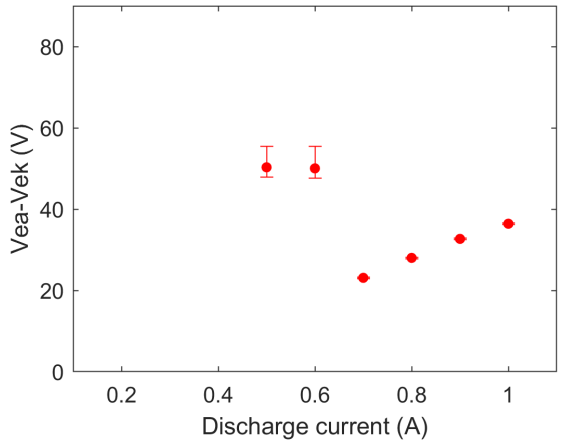

(c) Anode distance = 20 mm, flow rate = 10 sccm

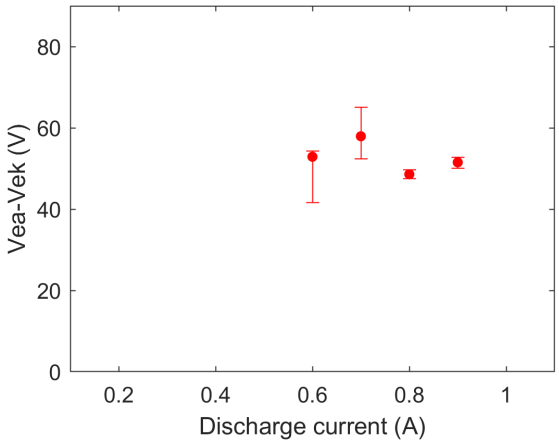

(d) Anode distance = 35 mm, flow rate = 11 sccm

Figure 4.3: Anode voltage minus keeper voltage versus discharge current at different anode distance and flow rates to decouple the emitter-keeper behavior from the discharge plume. Error bars show the range of values recorded over 5 ms.

A plume mode onset criterion has been found experimentally by Brophy *et al*, [3] in accordance with the general observation of extreme anode voltage oscillations during the plume mode operation. The criterion states that the anode peak-to-peak potential ($V_{a,pk-pk}$) is required to be over 5 V for the cathode to operate in plume mode. Figure 4.4 shows the VTHHC behavior with

the peak-to-peak anode potential criterion used for different flow rates, anode distances and discharge currents. In these plots, the blue line at 5 V represents the transition point from plume mode to spot mode, with the plume mode region lying above the blue line. The transition from plume to spot mode is sudden for all the cases and is observed visually as well as by changes in the discharge characteristics using the oscilloscope. The transition point for plume mode to spot mode increases with an increase in flow rate during VTHHC testing with krypton whereas Nikrant [2] pointed out that the transition from plume to spot mode for VTHHC testing with argon always occurred at discharge current of 2 A (see Figure 4.5), irrespective of the flow rate.

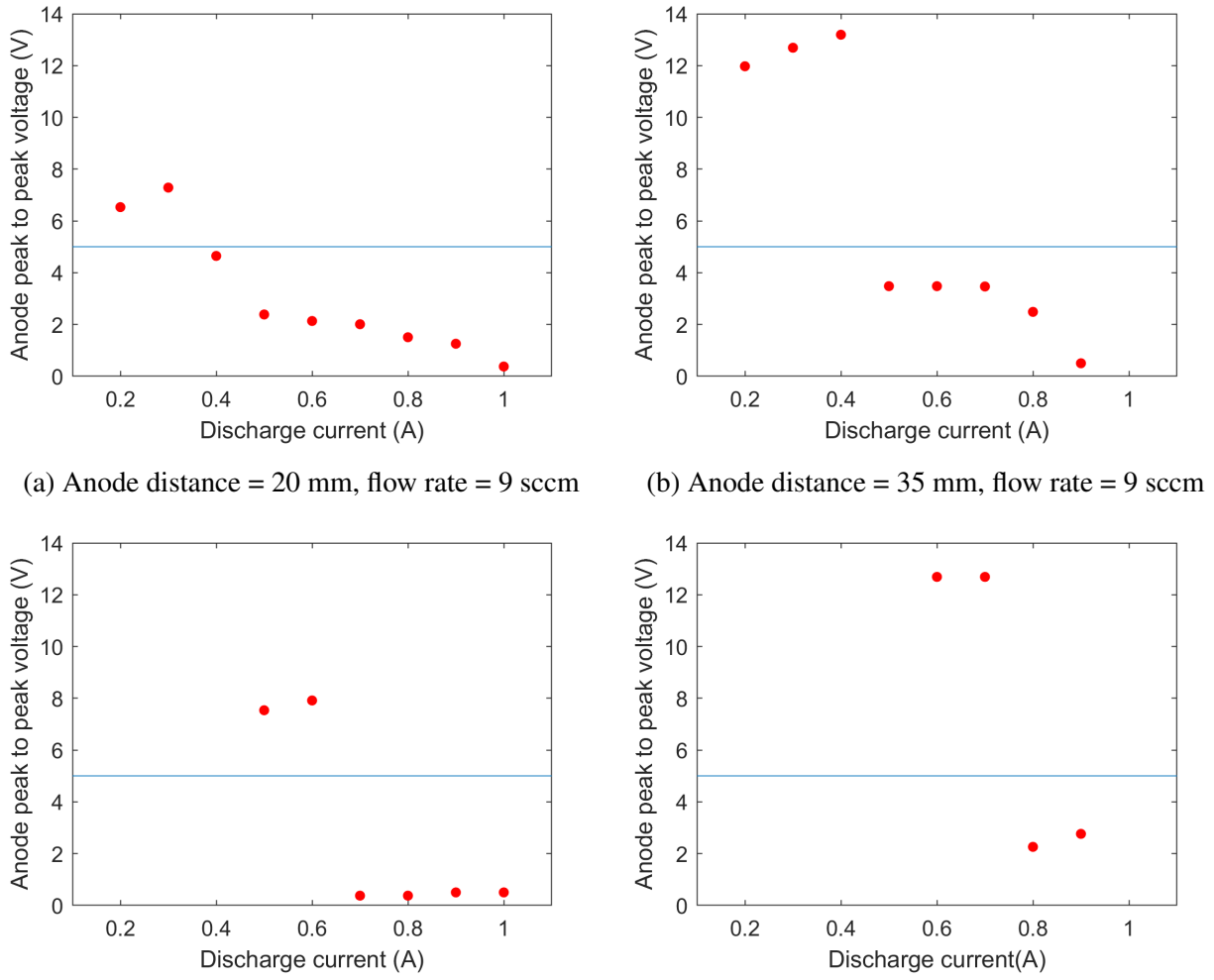

(a) Anode distance = 20 mm, flow rate = 9 sccm

(b) Anode distance = 35 mm, flow rate = 9 sccm

(c) Anode distance = 20 mm, flow rate = 10 sccm

(d) Anode distance = 35 mm, flow rate = 11 sccm

Figure 4.4: Peak-to-peak anode voltage oscillations versus discharge current at different anode distance and flow rates. The blue line at 5 V defines the Brophy criterion [3] with the cathode operating plume mode above 5 V and in spot mode otherwise.

Another interesting observation made during the VTHHC tests with argon was the slight in-

crease in the $V_{a,pk-pk}$ at 2.8 A for 13 and 15 sccm [2]. While the reason was unknown, this behavior was attributed to the hollow cathode operation in HCP mode at discharge currents greater than 2.5 A [2]. Extremely high $V_{a,pk-pk}$ oscillations were observed during this mode causing a permanent change in the discharge characteristics and excessive keeper erosion after the event [2]. This mode of operation is not attempted during VTHHC testing with krypton to avoid damaging the cathode, therefore the data points plotted in Figure 4.4 do not display this behavior.

Comparing Figures 4.4a and 4.4b, for the 9 sccm case at cathode-anode gaps of 20 mm and 35 mm exposes the effect of change in cathode-anode gap on the discharge characteristics. As the cathode-anode distance is increased from 20 mm to 35 mm the discharge mode transition point moves towards higher discharge currents. In other words, it can be said that the VTHHC changes to plume mode operation when the anode distance is increased. Although there is a need to collect more data at various cathode-anode distances and a constant discharge current to provide a more reliable observation, this observation is in accordance with the observations made in [52] for a 5 A-class LaB_6 cathode. According to Csiky [25], at a certain propellant feed rate, the cathode can operate in spot or plume mode for a range of anode distances based on the extent of electron emission, further supporting the above discussed observation and hypothesis. Additionally, comparing Figures 4.4a and 4.4b, it is seen that the peak-to-peak anode voltage scales with the cathode-anode distance. Further experimental data is required to solidify this observation and hypothesize the reason for this behavior.

The cathode plume during these tests show visual characteristics similar to those observed in [25], [12] and [26]. The cathode plume is observed from the top-left view port shown in Figure 3.1 and the images are captured using a Canon 80D camera. Figure 4.6a shows a photograph of the discharge plume in spot mode, at a flow rate of 9 sccm and cathode-anode gap of 20 mm, immediately after mode transition. Visually, a faint purple spot-like bright structure at the cathode orifice is visible. The light purple color of the plume suggests high density of krypton ions [12], which is a characteristic of the spot mode regime. The rest of the cathode-anode gap space appears dark due to ionization of the neutral krypton atoms near the keeper orifice plate. However, a brighter and focused plume instead of a bright spot-like structure is visible as the discharge current is increased after the transition point, shown in Figure 4.6b. It is observed that as the discharge current is increased, the plume grows brighter. At lower discharge currents, the discharge plume appears less-focused with the bright-spot still visible, see Figure 4.7. The plume has a divergence-angle as wide as the anode plate with the bright spot next to the keeper orifice plate. In comparison to the cathode tests with krypton, VTHHC testing with argon reported no sudden change in the appearance of the plume during the transition from plume to spot mode at 2 A [2]. Instead, the

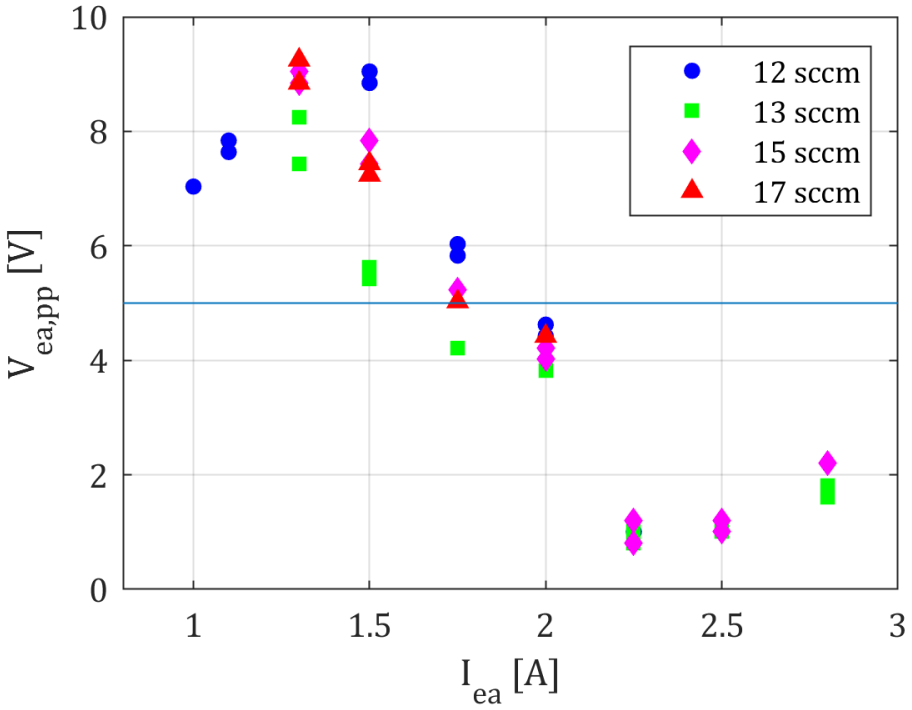

Figure 4.5: Peak-to-peak anode voltage oscillations versus discharge current at different flow rates for VTHHC testing with argon [2]. The blue line at 5 V defines the Brophy criterion [3] with the cathode operating plume mode above 5 V and in spot mode otherwise.

appearance of the plume became more luminous as the current was increased, similar to the cathode behavior with krypton as propellant.

A Fourier analysis of the keeper and anode voltages (same as those shown in Figure 4.2) is performed to provide additional insights regarding the main discharge behavior in different modes. For the voltage waveform plots, data is saved over a 5 ms period and every hundredth point is plotted using Matlab. Results obtained using the fast Fourier analysis in Matlab are plotted such that a 100 point moving average of the raw voltage data reduced the random noise while retaining sharp frequency peaks. Figures 4.8, 4.9, 4.10 and 4.11 show the voltage waveforms and fast Fourier transforms (FFT) for the 9 sccm case and 20 mm cathode-anode gap.

The plume mode (see Figure 4.8) exhibits a noisy spectrum, with small frequency peaks at 40 kHz and 90 kHz and the voltage waveforms are irregularly shaped, alternating within the range of 5 V for the anode and 10 V for the keeper. The anode and keeper voltage waveforms in Figure 4.8a appear to be anti-correlated with the change in keeper voltage approximately equal to twice the change in anode voltage. While the reason for this anti-correlation behavior is unclear, similar behavior is observed at other flow rates, discharge currents and cathode-anode distances as well.

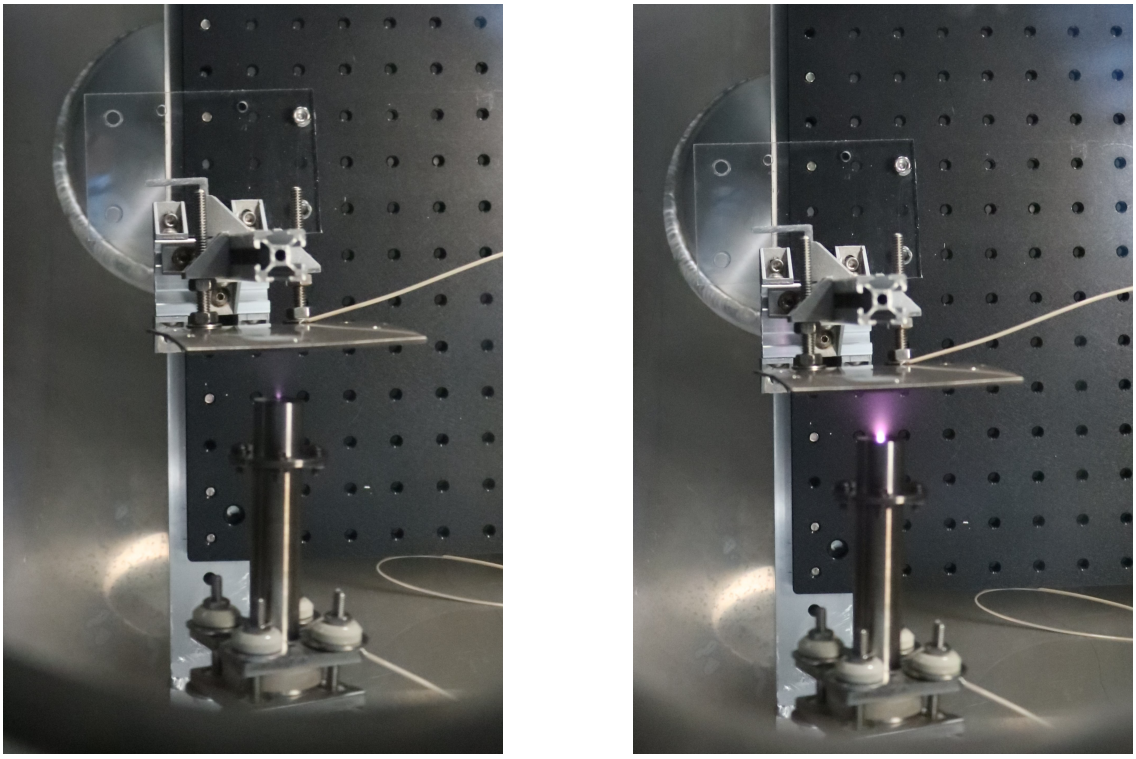

(a) (b)

Figure 4.6: Photographs of the main discharge for a cathode-anode gap value of 20 mm at 0.5 A (left) and 0.8 A (right) in spot mode. The discharge plume grows brighter as the discharge current is increased in the spot mode.

On the other hand, the spot mode (see Figure 4.9) shows a comparatively quiescent spectra. The voltage waveforms are irregular but alternate within a limit of less than 2 V, typical for spot mode operation. Similar to 4.8b, a small rise is observed at ≈100 kHz in Figure 4.9. Frequency peaks in the 40-100 kHz range are associated with the presence of ionization instabilities in the main discharge [52], [30]. Sary et al [53] suggest a mechanism for the generation of these instabilities, associating the high frequency (on the order of 1 MHz) component of the discharge voltage oscillations to extinguishing instabilities, and the low frequency to the movement of instabilities away from the cathode, at ion acoustic speeds.

The keeper voltage is observed to increase by ≈20 V with a comparatively noisier waveform during the spot mode operation at higher discharge currents. Typical for spot mode operation, the anode voltage waveform is substantially quieter at 1 A discharge current as compared to the voltage waveform at lower discharge currents. Recall that Figure 4.2 showed an abnormal behavior of the keeper voltage data points at higher discharge currents and an extremely low peak-to-peak anode voltage is observed in Figure 4.4. A peak is seen at 60 kHz for 0.9 A case (see Figure 4.10b)

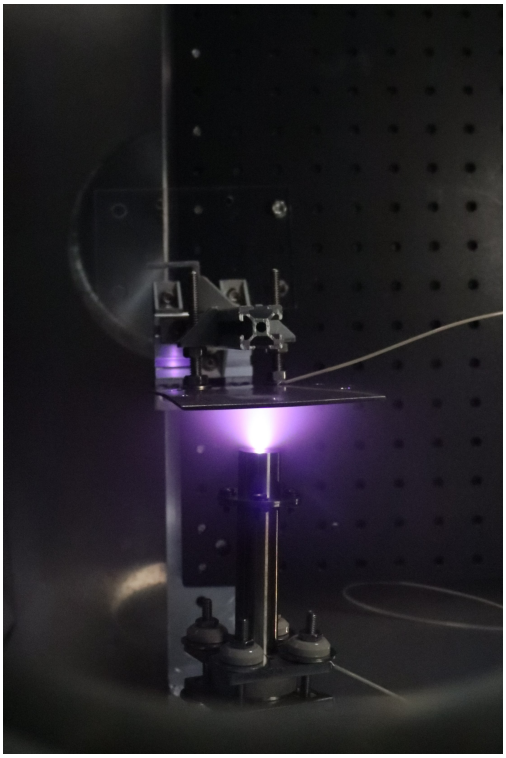

Figure 4.7: Photographs of the main discharge for a cathode-anode gap value of 20 mm at 0.3 A in plume mode.

that is present in both anode and keeper voltages. Furthermore, very sharp and distinct peaks are observed at 70 kHz, 142 kHz and 215 kHz for the 1 A case (see Figure 4.11b). These peaks are present in the keeper voltage but absent in the anode voltage suggesting the presence of an instability that does not couple with the main discharge. The sharpness of these frequency peaks implies resonant behavior. It can be hypothesized that these are the high frequency components of the voltage oscillations that excite and eventually quench an instability due to heating up of the electrons as suggested in [53]. The fact that these frequencies are absent at the anode voltage supports this hypothesis.

Similar FFT analysis was carried out by Nikrant [2] for the VTHHC with argon to study the oscillation behavior as the cathode transitioned from plume mode to spot mode and eventually to the HCP mode. For the case of 15 sccm flow rate and 1.6 A discharge current, a distinct frequency peak at 7-10 MHz was observed in the keeper voltage oscillations while being absent in the anode voltage curve. This suggested the presence of some higher frequency behavior internal to the cathode that does not couple to the plume plasma, similar to the VTHHC behavior with krypton at 1 A but at slightly lower frequencies. Based on this, it is anticipated that VTHHC operation with krypton at discharge currents above 1 A will result in HCP mode.

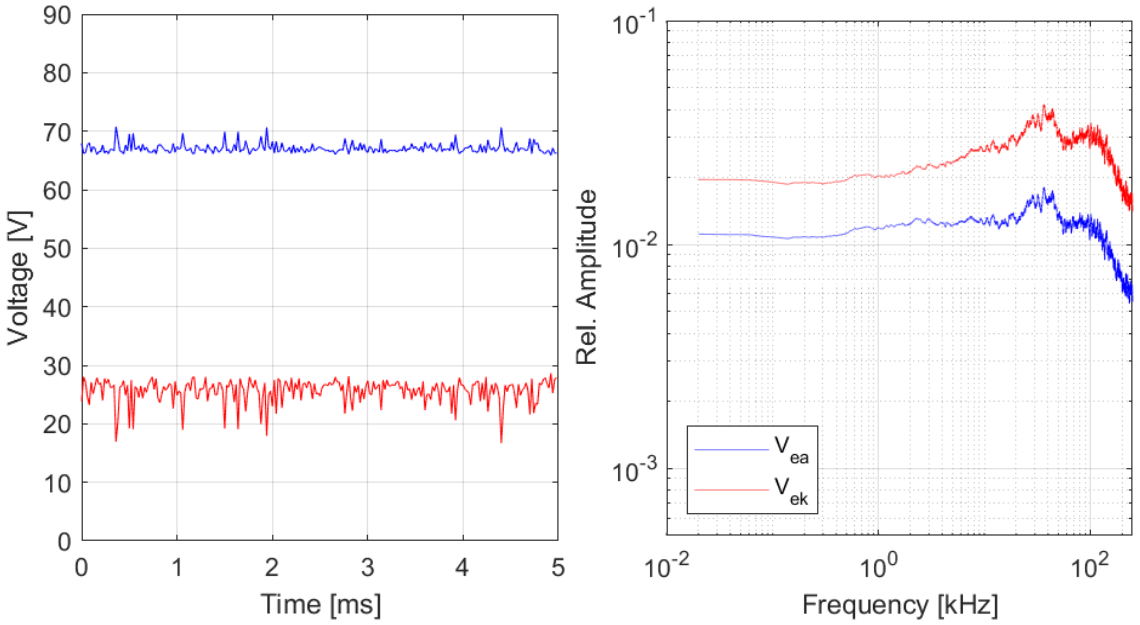

(a) (b)

Figure 4.8: Anode and keeper voltage waveforms and their FFT plots at 0.2 A, 9 sccm flow rate and 20 mm cathode-anode distance.

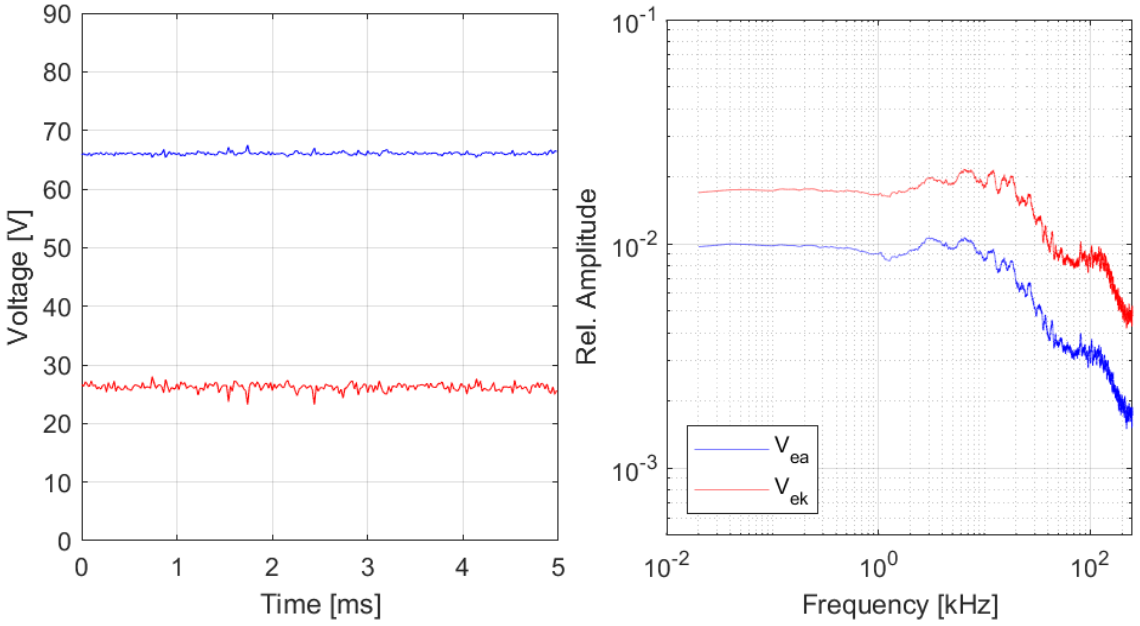

(a) (b)

Figure 4.9: Anode and keeper voltage waveforms and their FFT plots at 0.4 A, 9 sccm flow rate and 20 mm cathode-anode distance.

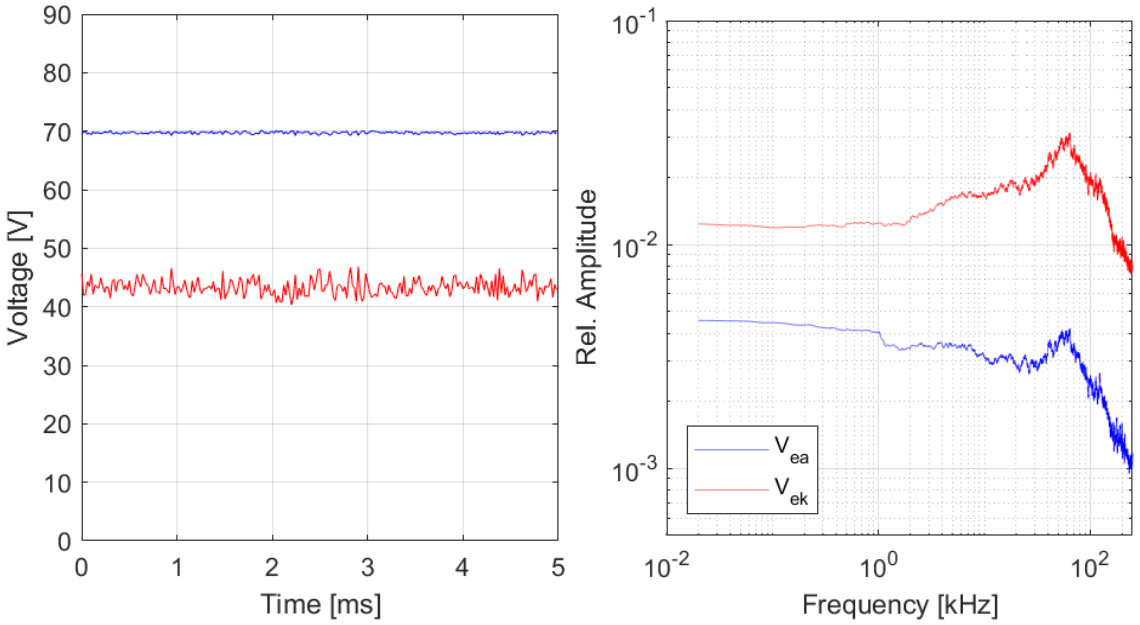

(a) (b)

Figure 4.10: Anode and keeper voltage waveforms and their FFT plots at 0.9 A, 9 sccm flow rate and 20 mm cathode-anode distance.

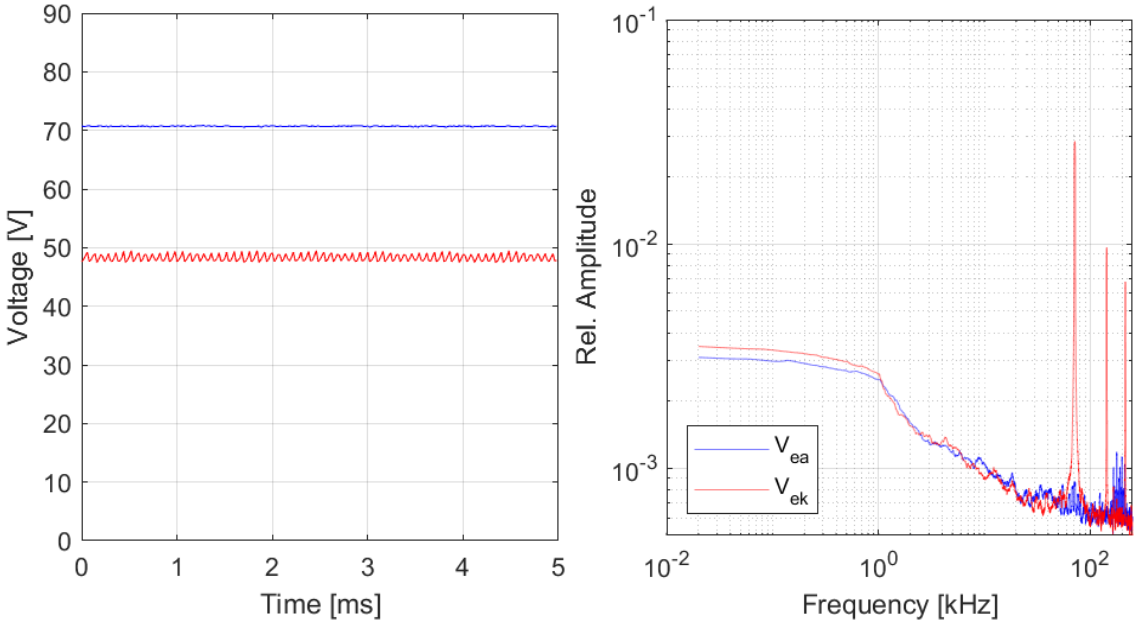

(a) (b)

Figure 4.11: Anode and keeper voltage waveforms and their FFT plots at 1 A, 9 sccm flow rate and 20 mm cathode-anode distance.

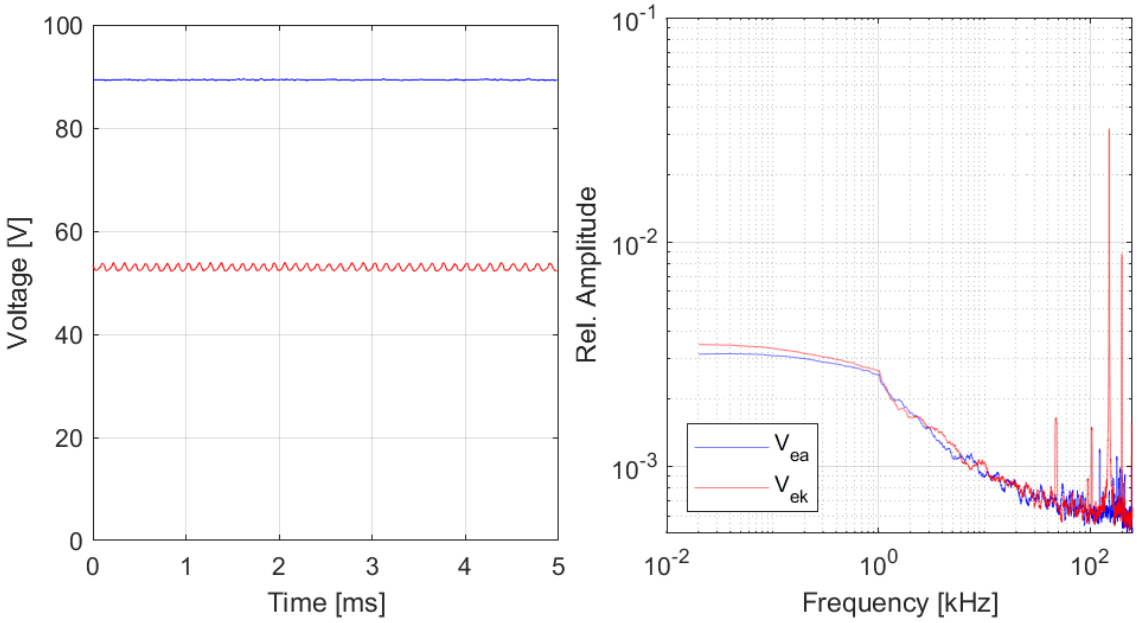

(a) (b)

Figure 4.12: Anode and keeper voltage waveforms and their FFT plots at 1 A, 10 sccm flow rate and 20 mm cathode-anode distance.

For the 10 sccm case at 20 mm cathode-anode gap, the voltage waveforms and FFT curves, during the plume mode, displayed behavior similar to that of the previously discussed 9 sccm case (see Figure 4.8). Interestingly, at discharge current 0.7 A and above, typical spot mode characteristics were entirely absent from the FFT curves but present in the voltage waveforms which presented only small voltage oscillations. Figure 4.12 shows the voltage waveform and FFT analysis result for 1 A discharge current case. A sharp and distinct peak is present at 150 kHz for the keeper voltage but absent in the anode voltage, suggesting resonant behavior as discussed previously for the 9 sccm case, both at 1 A discharge current. This erratic behavior is evident from the plots in 4.4 and 4.3 where the anode current is extremely low.

To study the effect of varying cathode-anode gap, similar analysis is carried out for voltage data recorded at 9 sccm and 11 sccm for 35 mm cathode-anode distance case. The fundamental peaks appear within the same range of 40-100 kHz but broader and are observed for both, spot and plume mode, concurring with the findings of Potrivitu et al. [52]. Additionally, during the spot mode operation, the FFT curves appeared to be more quiescent compared to those for 20 mm cathode-anode gap. Figures 4.13b and 4.14b show the voltage waveforms and the fast Fourier analysis results for 9 and 11 sccm at discharge current 0.9 A and a cathode-anode gap of 35 mm. Although these results are promising and suggest that the cathode operates more stably for the 35

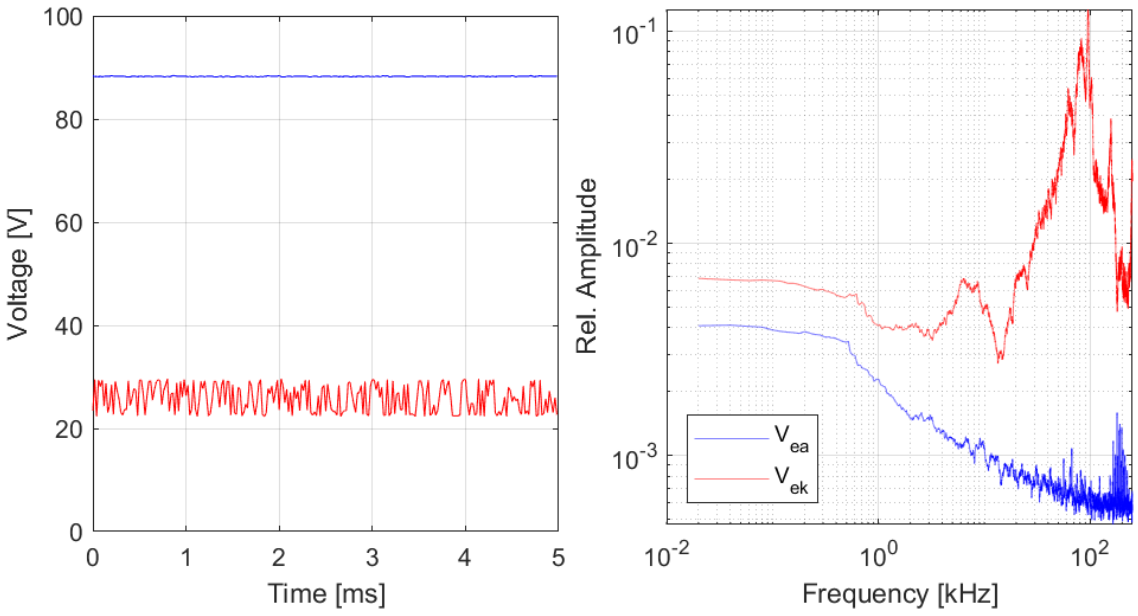

(a) (b)

Figure 4.13: Anode and keeper voltage waveforms and their FFT plots at 0.9 A, 09 sccm flow rate and 35 mm cathode-anode distance.

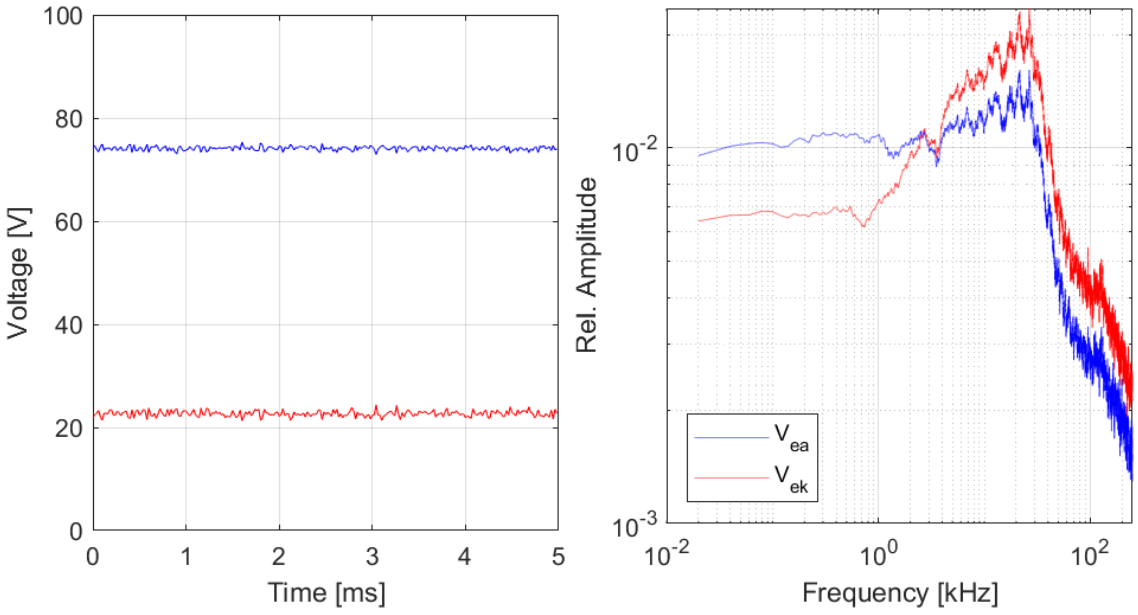

(a) (b)

Figure 4.14: Anode and keeper voltage waveforms and their FFT plots at 0.9 A, 11 sccm flow rate and 35 mm cathode-anode distance.

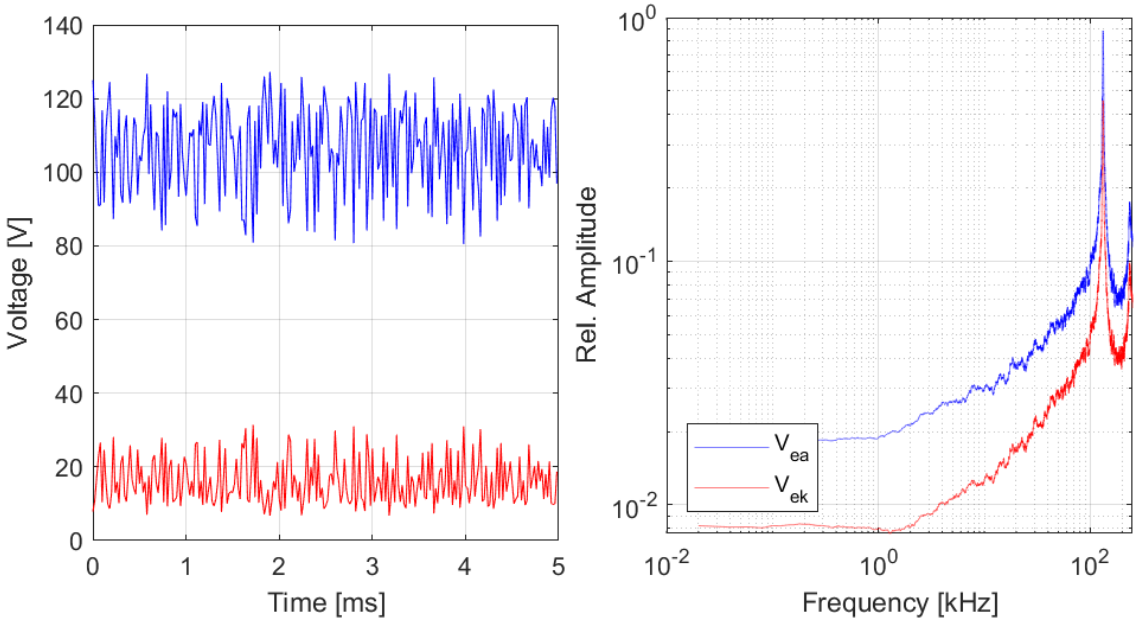

(a) (b)

Figure 4.15: Anode and keeper voltage waveforms and their FFT plots at 9 sccm flow rate and 5 mm cathode-anode distance.

mm cathode-anode gap, more tests are required to effectively hypothesize the effect of cathode-anode gap on the discharge modes and to find the best anode position for VTHHC operation.

Section 4.1 discusses the event of anode glowing when the cathode-anode gap is set to 5mm. Voltage waveforms and FFT analysis for this case, shown in Figure 4.15 revealed some very interesting features. Recall that the anode power supply is voltage limited to 130 V, Figure 4.15a shows that the anode voltage reached the power supply limit unlike the cases previously discussed. Additionally, the voltage oscillations for both keeper and anode voltages were violent and within a limit of 20-50 V. This behavior has been associated with the acceleration of ion to high energies in similar experiments [30]. FFT analysis of the voltage waveforms show a distinct peak at 130 kHz. According to Goebel *et al*, "These oscillations can range from ionization instabilities to turbulent ion acoustic waves and can interact with the anode power supply to cause unstable operation", which is observed during the tests carried out at 5 mm cathode-anode gap. An unstable bluish plume is observed during this test, seen in Figure 4.16, suggesting a strong presence of excited neutral krypton atoms in place of ions [12]. At low mass flow rates, the anode voltage rises and becomes unstable with large temporal variations due to high current production, which is limited by the low plasma density [12]. Electron attracting sheaths may be form in such scenarios, increasing the total collected current at the anode which may have led to the heating up and glowing of anode

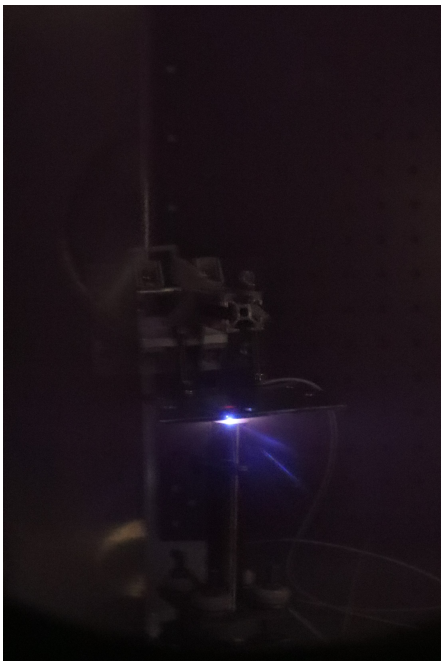

Figure 4.16: Photograph of the main discharge for cathode-anode gap value of 5 mm in plume mode. Note that the discharge plume is partially obscured by the anode plate.

[52].

4.4 Plasma model and results

By making several common assumptions about the discharge in a hollow cathode, Nikrant [2] combined several hollow cathode plasma models to simultaneously calculate plasma parameters using only two unobstrusively measured quantities: discharge current and emitter-keeper voltage. The discharge current is directly controlled via the anode power supply and the emitter-keeper voltage is uncontrolled and results from the discharge properties. A detailed explanation for the derivations and equations utilized in the plasma model are discussed in Nikrant's thesis [2].

The plasma length, L is taken to be the emitter-keeper gap of 1.27 mm and r_e is taken to equal the emitter radius, equal to 3.4 mm. The charge state of the plasma, Z is set to 1 due to the presence of low energy electrons in the cathode plasma. The plasma attachment length is assumed to be roughly equal to half of the emitter length, 5 mm for VTHHC, yielding the plasma attachment area, A. The electron temperature is chosen by multiplying 1 eV, the commonly assumed electron temperature for hollow cathodes with xenon as propellant, by the ratio of ionization potentials for krypton and xenon [36]. The above assumptions resulted in considerable values for thermionic emission current, plasma density, emitter temperature, emitter heat loss and α. Nikrant in [2]

mentions that the value of α, affecting the ratio of ion to thermionic electron currents, is arguably the most important result of this analysis. The value of α obtained using this plasma model were greater than the commonly assumed value of 2, meaning that the ion impingement current at the emitter is a critical portion of the total discharge current. This observation aligns with [1], which states that ion bombardment is the dominant self-heating mechanism in an open-ended emitter configuration.

The experimental data collected during VTHHC testing with krypton is provided as input to the plasma model. The results are shown in Figures 4.17 to 4.21. The plot legend remains the same for all the plots.

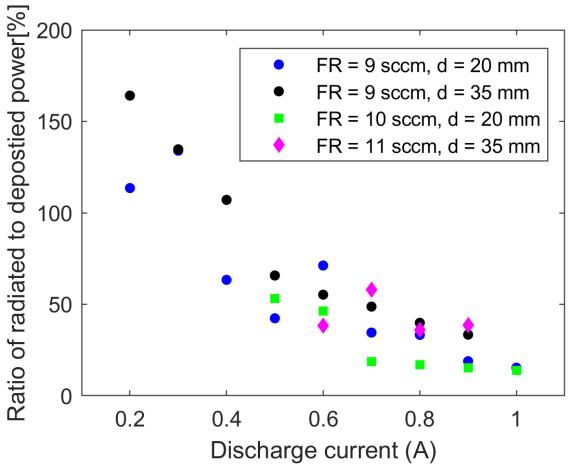

Figure 4.17: Ratio of radiated power to deposited power for the emitter (%) versus discharge current at varying flow rates and cathode-anode distances with krypton, predicted by plasma model.

It is evident from Figure 4.17 that both the radiated and the deposited power decrease with an increase in the discharge current. While the model predicts radiated power values less than 10 W, this is not the case in reality. Although some quantity of power is radiated by the discharge plume plasma, a substantial quantity is radiated by the cathode to the surroundings. As discussed earlier, the cathode extinguished due to insufficient heating and unstable thermal behavior which is partially caused due to excess power being radiated. This issue is taken care of using the heater and heat shields in conventional cathodes. While the cathode researched in this work is a heaterless cathode, it is believed that using tantalum or any high refractory-metal foil as a heat shield can improve the cathode behavior and operation [14].

Figure 4.18 shows emitter surface temperatures in the range of 1240 to 1360 degree Celsius, increasing with an discharge current. Although the assumption of electron temperature as a constant limits the credibility of these values to some extent, the emitter surface temperature values

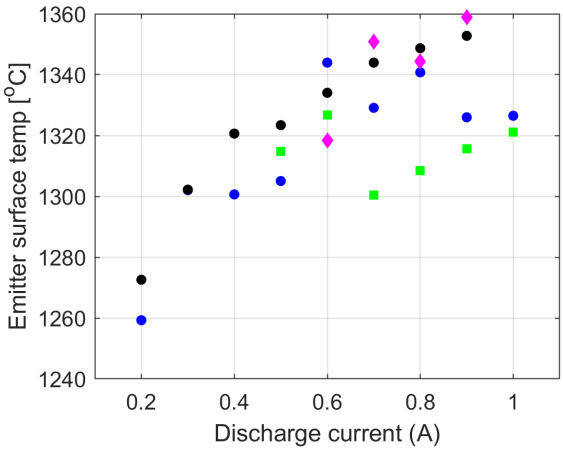

Figure 4.18: Emitter surface temperature versus discharge current at varying flow rates and cathode-anode distances krypton, predicted by plasma model. The legend for this plot is the same as that for Figure 4.17.

shown in the plot are close to the reported thermocouple reading of 1258 degree Celsius at the emitter in [12] for a LaB_6, 1 A-class cathode with krypton. This observation strongly agrees with the temperature value predicted by the plasma model for VTHHC operation, at discharge currents less than or equal to 1 A, with krypton.

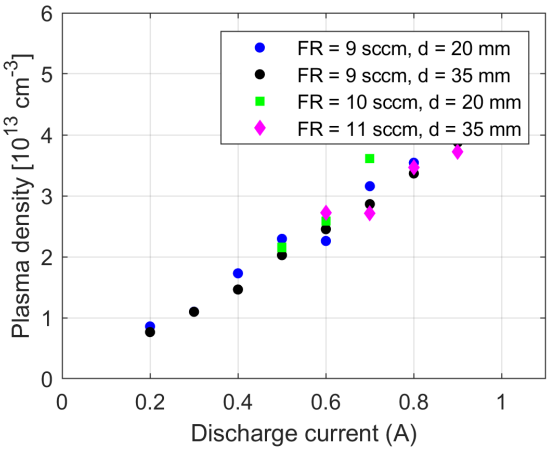

Figure 4.19: Plasma density vs discharge current at varying flow rates and cathode-anode distances krypton, predicted by plasma model. The legend for this plot is the same as that for Figure 4.17.

Figure 4.19 shows the plasma density in the range of 1-6 x 10^{-13} cm^{-3}, in accordance with the generally observed values. The plasma density is seen to increase almost linearly with an increase in the discharge current, but the change in mass flow rate does not seem to effect it. This

is in disagreement with the generally observed cathode plasma characteristics, where the plasma density is affected by the flow rate and discharge modes. An increase in flow rate pushes the plasma towards the exit, in turn reducing the effective emission length. This leads to the hypothesis that because this model assumes a constant emission length and electron temperature, the simulation fails to account for the effect of these parameters on the plasma density.

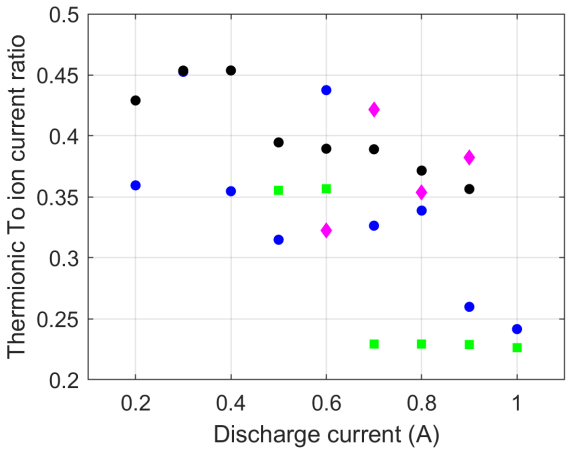

Figure 4.20: Ratio of thermionic to ion current vs discharge current at varying flow rates and cathode-anode distances krypton, predicted by plasma model. The legend for this plot is the same as that for Figure 4.17.

The plot for the ratio of thermionic current to ion current appears to be scattered and roughly follows the same trend as the keeper voltage. The thermionic current in a hollow cathode depends on the electron temperature and the plasma attachment length. Although the plasma model assumes the plasma electron temperature and attachment length to be constant, these parameters change during the hollow cathode operation. The lack of trend in this plot may be due to this assumption made in the plasma model.

The electron Mach number is calculated to be the ratio of electron drift velocity to thermal velocity [1] and plotted in Figure 4.21. Accounting for the model limitations, it is safe to say that electron Mach numbers higher than 1 were observed at high discharge currents. The nonequilibirum ionization nature of plasma discharge at electron Mach numbers greater than 1 creates an ideal bed for the development of various plasma instabilities [12], [1]. This supports the earlier discussion in Section 4.3, suggesting the presence of ionization instabilities and ion acoustic turbulence, where the generation of the latter depends on the former [12].

Using the parameters calculated using the plasma model, electron plasma frequency , ion acoustic frequency and frequencies for Buneman instability are calculated using the formulas in

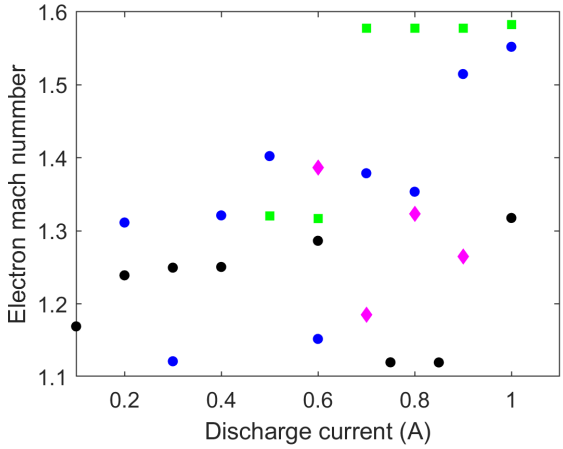

Figure 4.21: Electron Mach number versus discharge current at varying flow rates and cathode-anode distances krypton, predicted by plasma model. The legend for this plot is the same as that for Figure 4.17.

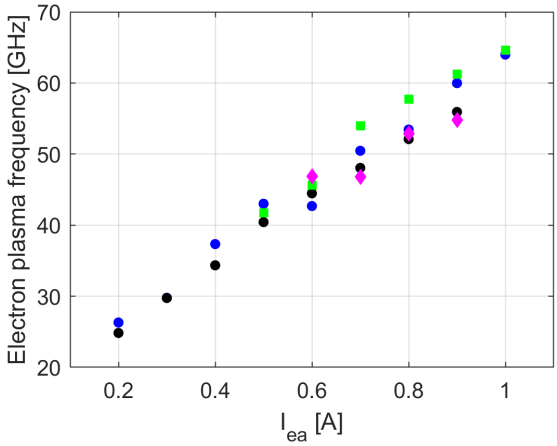

Figure 4.22: Electron plasma frequency (GHz) versus discharge current at varying flow rates and cathode-anode distances krypton, predicted by plasma model. The legend for this plot is the same as that for Figure 4.17.

[54] and the plasma density values predicted by the plasma model (see Figure 4.19). Figure 4.22 shows electron plasma frequency in the range of 25-65 GHz and is observed to increase linearly with an increase in discharge current. At Mach numbers greater than 1 (see Figure 4.21) both Buneman and ion acoustic instabilities can develop. Buneman instability is believed to arise from a relative drift between electrons and ions and the calculated frequency is shown in Figure 4.23. The Buneman instability frequency plot shows the same trend as the electron plasma frequency with the frequency values two orders of magnitude lower than the electron plasma frequency. Fig-

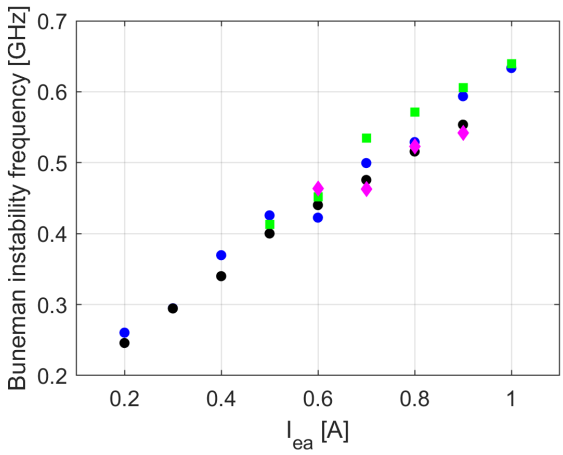

Figure 4.23: Buneman instability frequency (GHz) versus discharge current at varying flow rates and cathode-anode distances krypton, predicted by plasma model. The legend for this plot is the same as that for Figure 4.17.

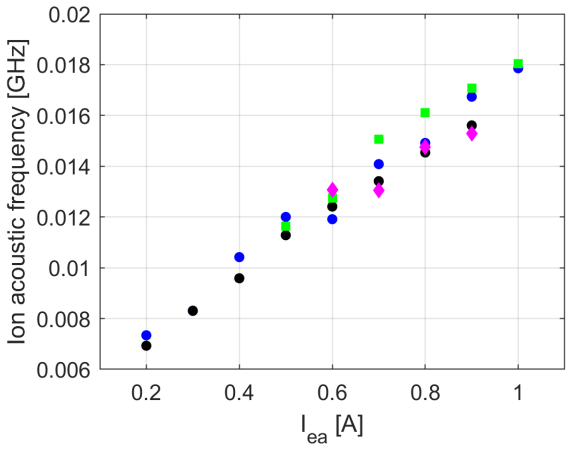

Figure 4.24: Ion acoustic frequency (GHz) versus discharge current at varying flow rates and cathode-anode distances krypton, predicted by plasma model. The legend for this plot is the same as that for Figure 4.17.

ure 4.24 shows that the ion acoustic frequency follows a similar trend to the previous plots but the frequency values are comparatively very low and lie within the range of 7-18 MHz. Compared to the resonant frequencies observed in Section 4.3, these calculated frequencies appear to be very high. Further analysis and experiments are required to probe the resonant behavior of the discharge plume in spot and plume mode.

The plots discussed in this section validate the capability of this model to reasonably predict plasma properties in agreement with the commonly observed cathode behavior. The limitations of

this model arise due to the electron temperature and plasma attachment length assumptions. This is because these quantities are believed to change with varying flow rates and discharge currents [2].

4.5 Post-experiment visual inspection

Post-test visual inspection of the cathode is carried out using a microscope to study the extent of keeper and emitter erosion as well as emitter poisoning. Figure 4.25 shows the downstream end of the LaB_6 over the duration of four days of testing. Figure 4.25a shows the downstream face of the emitter before any tests were carried out. A rainbow colored pattern is seen on the face of the emitter (see Figures 4.25b and 4.25c). This may have occurred because of lanthanum oxide (La_2O_3) build-up on the emitter surface due to thermal oxidation. High temperatures usually lead to rapid oxide growth, forming a layer on the surface. As light passes through this oxide layer, it is reflected off the emitter surface but some is also reflected from the surface of the oxide, exhibiting the rainbow pattern. This suggests that a very thin layer of oxide is formed during the initial tests. This white colored La_2O_3 coverage grew more evident on the last day of testing, see Figure 4.25d. The amount of La_2O_3 formation is less compared to the observation made in [2] during previous VTHHC testing, supporting the hypothesis that minor improvements in the clamp design and setup have reduced the extent of emitter poisoning.

Radial fractures are observed in the downstream emitter tube. Thermal shocks due to change in electron and plasma temperature during the different discharge modes may have led to the development of these fractures. The bright purple spots visible in these microscope images are believed to be the areas of arc attachment, similar to observations made in [2]. Localized heating due to arcing during arc attachment likely eliminates the La_2O_3 deposit [2]. Interestingly, the emitter erosion phenomenon observed during previous VTHHC testing [2] is not observed here. Consequently, the melted tantalum deposits at the end of the cathode tube observed in [2] are absent during the cathode operation with krypton. This could be because operation of cathode in the HCP mode is not attempted during the VTHHC tests with krypton.

The hypothesis introduced by Nikrant in [2] regarding the significant coverage of La_2O_3 at the upstream end of the emitter as compared to the downstream end is found to be true during the current tests as well. The increased temperature and plasma exposure at the downstream face of the emitter removes some of the La_2O_3 as it forms while the upstream face is significantly covered in La_2O_3 (see Figure 4.26).

Figure 4.27 shows the image of the inner-side of the keeper orifice plate before and after the

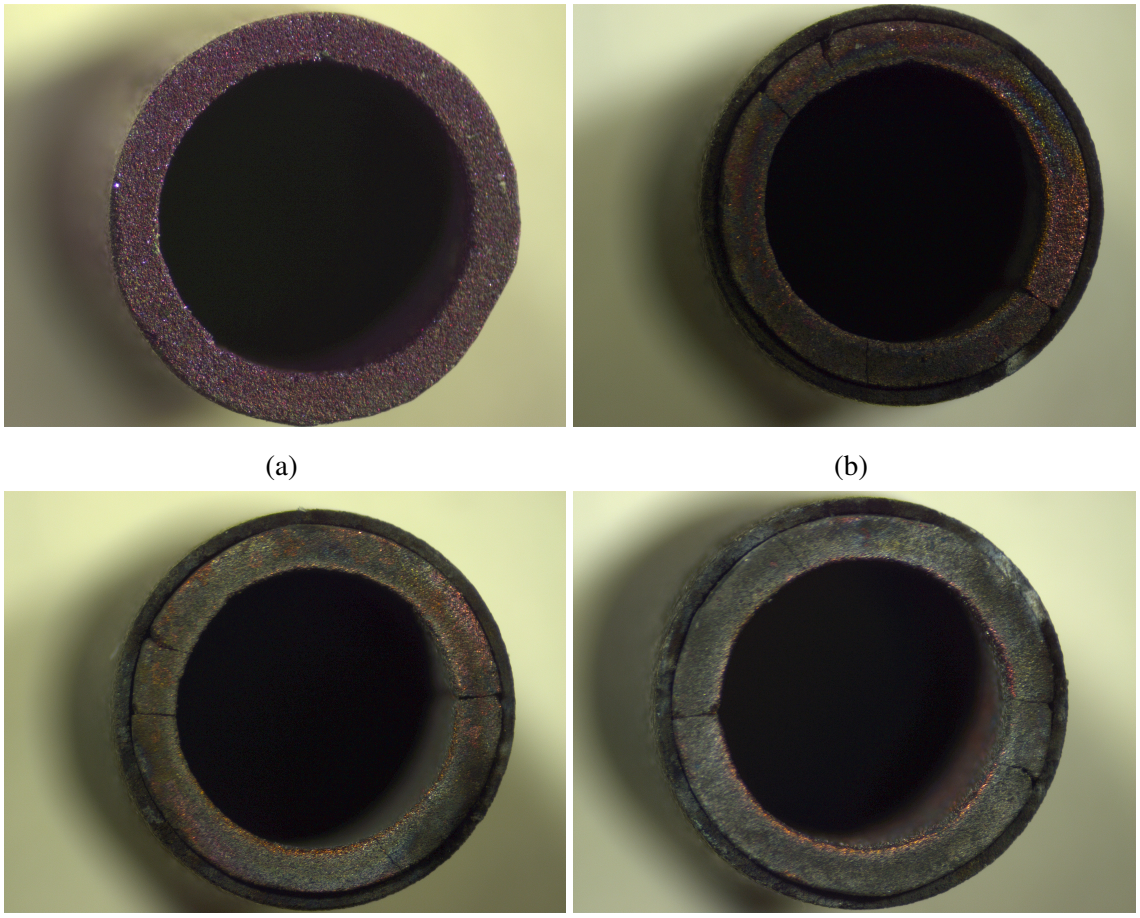

(a) (b)

(c) (d)

Figure 4.25: Microscope images of the downstream end of the emitter over four days of testing.

tests. The keeper saw substantial erosion during the previous VTHHC testing in the HCP mode [2] and because the same keeper is utilized for the current research, it is difficult to comment on the extent of erosion. The crater-like surface before and after the tests appears to be similar. The yellowish-green deposit is believed to be tungsten oxide because of the tungsten spring which holds the emitter at the end of the cathode tube. Deposit of a similarly colored material was observed in [2], supporting the hypothesis. The plasma-facing keeper orifice is observed to undergo significant chamfering, seen in Figure 4.28. Literature explains that an increase in the discharge current enhances the voltage amplitude fluctuations, increasing the number and energy of ions which leads to significant keeper erosion [31]. Additionally, Pedrini *et al.* [51] observed that ion bombardment can damage the orifice aspect ratio, while the shape can appear intact. Because it is difficult to visually observe these changes, a profile analysis of the VTHHC keeper may be helpful to observe the change in aspect ratio.

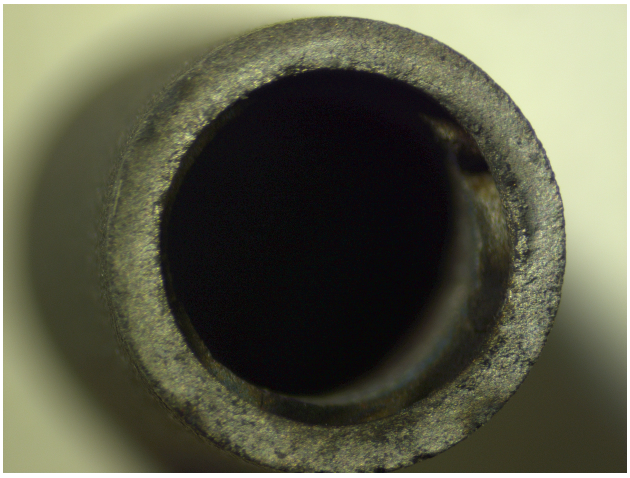

Figure 4.26: Microscope image of the upstream end of the emitter.

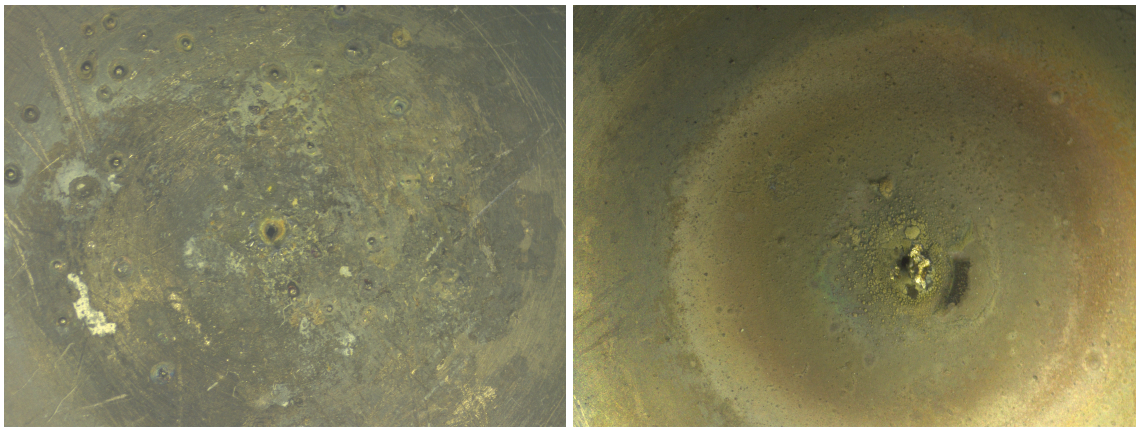

(a) (b)

Figure 4.27: Pre-test and post-test microscope images of keeper inner-side.

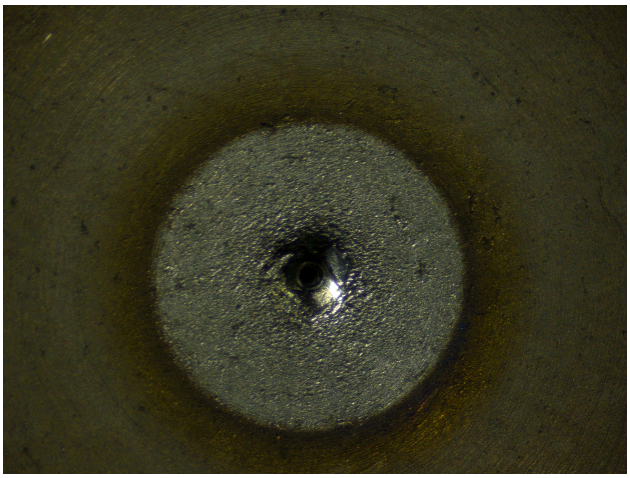

Figure 4.28: Microscope images of the chamfered keeper orifice.

Chapter 5

Conclusions and Future Research

5.1 Experimental conclusions

A first-generation heaterless LaB_6 hollow cathode is developed and tested in stand-alone configuration. An external anode plate, placed over a range of distances from the cathode exit plane, is used to characterize the cathode performance. This work focuses on the investigation of cathode performance with krypton, and the effect of cathode-anode gap value and flow rates on the mode transition process.

Krypton is found to be suitable for operation at current lower than 1 A, with keeper voltages as high as 400 V to initiate breakdown followed by a glow discharge to warm up the cathode. During the main discharge, keeper and anode voltages are lowered down to tens of volts only. For the tests discussed here, the discharge current is between 0.2 and 1 A with the krypton mass flow rate set between 9 and 11 sccm. Voltage-current plots show typical hollow cathode characteristics with a few anomalies. The cathode displays plume mode operation at low discharge currents, spot mode operation at higher discharge current and hints towards high current plume mode as the discharge current neared 0.9 A. Frequency peaks in the range of 40-150 kHz are seen during the plume mode and during spot mode at very high discharge currents, suggesting resonant behavior that can be attributed to plasma instabilities arising due to propellant ionization.

The cathode-anode gap is varied from 5 to 35 mm and the discharge mode is observed to change from spot to plume mode. Overall, the FFT curves reveal a broader and denser frequency spectra with many peaks in the frequency space at larger anode distances. During the spot mode operation, the FFT curve appears to be more quiescent as the anode distance is increased. On the other hand, during the plume mode operation, an increase in anode voltage is observed.

Visual observations of the discharge plume show typical cathode characteristics with a bright

spot-like structure present during the spot mode and a more diffused plume is observed during the plume mode. The transition from plume to spot mode is sudden for all the discussed cases. This transition was observed visually and verified using the Brophy criterion which states that cathode operates in plume mode at peak-to-peak anode voltages above 5 V.

Plasma properties predicted using the plasma model are close to the expected range for hollow cathodes and therefore validate the plasma model as well as highlight the implications of its limitations. Also, post-test visual observation of the cathode components using a microscope is carried out. In spite of the improvements to mitigate leaks in the cathode structure and the overall system, a small amount of La_2O_3 coverage is still observed. Keeper erosion is observed with the keeper orifice slightly chamfered. Lastly, the appearance of longitudinal fractures in the emitter tube suggests the requirement of a refractory metal foil to mitigate the radiation losses and protect the emitter from thermal shocks.

5.2 Future work

While some interesting observations regarding the effects of varying discharge current, flow rate, and cathode-anode gap were made during the presented research, there is a need to conduct similar experiments at a wider range of cathode-anode gap and flow rate to fully understand the VTHHC behavior and predict optimum parameters for efficient VTHHC operation. The scaling of peak-to-peak anode voltage with cathode-anode gap in relation to the electric field in the cathode-anode gap needs to be studied further.

Section 4.3 discussed the discharge behavior during spot and plume mode, wherein distinct peaks were seen in the range of 40-150 kHz, hinting at the presence of various plasma instabilities during the plume mode operation. Further, measurements of spatially resolved plasma properties, using probes, are required to propose the cause of cathode discharge behavior in different modes, to identify the resonant behavior seen at various frequencies, and to minimize keeper erosion. Detailed study of plasma properties in the cathode internal and external region is required to shed light on the decoupling of anode and keeper voltage at high discharge currents and the onset of the HCP mode. Additionally, the anti-correlation of anode and keeper voltages needs to be probed further to understand this interesting phenomenon. Section 4.4 validates the unique plasma model presented by Nikrant in [2]. While the model provides reasonable values of the plasma parameters, curbing its limitations by using time-dependent electron temperature measurements or emitter surface temperature measurements can increase its accuracy.

Additionally, the unstable thermal behavior of the cathode during steady-state operation de-

mands the use of a heat shield to protect the emitter thermally. Improvements in the design are required to eliminate the leaks in the cathode structure, incorporate thermocouples for easy instrumentation and to allow quick modifications of the cathode tube-keeper gap as well as the keeper orifice geometry.

The VTHT with Halbach array design idea (see Appendix A) is a unique and novel idea, presenting an opportunity for designing efficient Hall thrusters with lower power consumption and a strong, controllable magnetic field. It is the hope of the author that these ideas will be pursued in future, answering the questions about the plasma dynamics, plume morphology and leading to the development of a state-of-the-art electric propulsion system at Virginia Tech.

Bibliography

[1] D. M. Goebel and I. Katz, *Fundamentals of Electric Propulsion: Ion and Hall Thrusters*. Wiley, 2008.

[2] A. Nikrant, "Development and modelling of a low current lab_6 heaterless hollow cathode," Master's thesis, Virginia Polytechnic Institute and State University, July 2019.

[3] J. Brophy, D. Brinza, J. Polk, and M. Henry, "The dsi hyper-extended mission," in *Joint Propulsion Conference*, 2002.

[4] J. Szabo, R. Tedrake, G. Kolencik, and B. Pote, "Measurements of a krypton fed 1.5 kw hall effect thruster with a centrally located cathode," in *International Electric Propulsion Conference*, October 2017.

[5] E. Y. Choueiri, "Plasma oscillations in hall thrusters," *Physics of Plasmas*, vol. 8, pp. 1411–1426, Apr. 2001.

[6] R. G. Jahn and E. Y. Choueiri, *Encyclopedia of Physical Science and Technology*. New York: Academic Press, 2002.

[7] Wikipedia contributors, "Plagiarism — Wikipedia, the free encyclopedia," 2019. [Online; accessed 29-March-2020].

[8] J.-P. Boeuf, "Tutorial: Physics and modeling of hall thrusters," *Journal of Applied Physics*, vol. 121, p. 011101, Jan. 2017.

[9] H. Hwang-Jin, "Physical processes in hollow cathode discharge," Master's thesis, Naval Postgraduate School, 1989.

[10] M. T. Domonkos, A. D. Gallimore, G. J. Williams, and M. J. Patterson, "Low-current hollow cathode evaluation," *American Institute of Aeronautics and Astronautics*, 1999.

[11] M. Mandell and I. Katz, "Theory of hollow operation in spot and plume modes," in *30th Joint Propulsion Conference and Exhibit*, Jun 1994.

[12] G.-C. Potrivitu, L. Xu, S. Huang, M. W. A. B. Rohaizat, and S. Xu, "Discharge mode transition in a krypton-fed 1 a-class lab6 cathode for low-power hall thrusters for small satellites," *Journal of Applied Physics*, vol. 127, February 2020.

[13] D. Pedrini, R. Albertoni, F. Paganucci, and M. Andrenucci, "Theoretical model of a lanthanum hexaboride hollow cathode," *IEEE Transactions on Plasma Science*, vol. 43, pp. 209–217, November 2014.

[14] D. Lev and L. Appel, "Heaterless hollow cathode technology - a critical review," in *Space Propulsion 2016*, May 2016.

[15] C. J. Wordingham, P.-Y. C. R. Taunay, and E. Y. Choueiri, "Theoretical prediction of the dense-plasma attachment length in an orificed hollow cathode," 2017.

[16] I. Langmuir, "The interaction of electron and positive ion space charges in cathode sheaths," *Physical Review*, vol. 33, 1929.

[17] O. Richardson, "Electron theory of matter," *Philips Magazine*, vol. 23, pp. 594–627, 1912.

[18] W. Kohl, *Handbook of Materials and Techniques for Vacuum Devices*. New York: Reinhold, 1967.

[19] W. Schottky, "Concerning the discharge of electrons from hot wires with delayed potential," *Annalen der Physik*, vol. 44, pp. 1011–1032, July 1914.

[20] J. M. Lafferty, "Boride cathodes," *Journal of Applied Physics*, vol. 22, pp. 299–309, Mar 1951.

[21] R. Levi, "Improved impregnated cathode," *Journal of Applied Physics*, vol. 26, p. 639, 1955.

[22] J. Cronin, "Practical aspects of modern dispenser cathodes," *Microwave Journal*, vol. 22, pp. 57–62, September 1979.

[23] H. E. Gallagher, "Poisoning of LaB6 cathodes," *Journal of Applied Physics*, vol. 40, pp. 44–51, Jan 1969.

[24] V. K. Rawlin and E. V. Pawlik, "A mercury plasma-bridge neutralizer," *Journal of Spacecraft and Rockets*, vol. 5, pp. 814–820, Jul 1968.

[25] G. A. Csiky, "Measurements of some properties of a discharge from a hollow cathode," tech. rep., NASA Lewis Research Center, 1969.

[26] I. G. Mikellides, P. Guerrero, A. L. Ortega, and J. E. Polk, "Spot-to-plume mode transition investigations in the hermes hollow cathode discharge using coupled 2-d axisymmetric plasma-thermal simulations," in *2018 Joint Propulsion Conference*, American Institute of Aeronautics and Astronautics, Jul 2018.

[27] S. E. Cusson, B. A. Jorns, and A. Gallimore, "Ion acoustic turbulence in the hollow cathode plume of a hall effect thruster," in *2018 Joint Propulsion Conference*, American Institute of Aeronautics and Astronautics, Jul 2018.

[28] D. Fearn and C. Philip, "An investigation of physical processes in a hollow cathode discharge," in *9th Electric Propulsion Conference*, International Electric Propulsion Conference, American Institute of Aeronautics and Astronautics, Apr. 1972.

[29] M. P. Georgin, B. A. Jorns, and A. Gallimore, "Plasma instabilities in the plume of a hollow cathode," in *2018 Joint Propulsion Conference*, American Institute of Aeronautics and Astronautics, Jul 2018.

[30] D. M. Goebel, K. K. Jameson, I. Katz, I. G. Mikellides, and J. E. Polk, "Energetic ion production and keeper erosion in hollow cathode discharges," in *International Electric Propulsion Conference*, October 2005.

[31] D. M. Goebel, K. K. Jameson, I. Katz, and I. G. Mikellides, "Potential fluctuations and energetic ion production in hollow cathode discharges," *Physics of Plasmas*, vol. 14, August 2007.

[32] R. F. Kemp and D. F. Hall, "Ion beam diagnostics and neutralization," tech. rep., TRW systems, 1967.

[33] D. M. Goebel, K. K. Jameson, I. Katz, and I. Mikellides, "Plasma potential behavior and plume mode transitions in hollow cathode discharges," in *30th International Electric Propulsion Conference*, American Institute of Aeronautics and Astronautics, Jan. 2007.

[34] M. P. Georgin, B. A. Jorns, and A. Gallimore, "An experimental and theoretical study of hollow cathode plume mode oscillations," in *35th International Electric Propulsion Conference*, 2017.

[35] L. A. Rehn, "Argon hollow cathode," Master's thesis, Colorado State University, 1976.

[36] L. Rehn and H. Kaufman, "Correlation of inert gas hollow cathode performance," in *13th International Electric Propulsion Conference*, American Institute of Aeronautics and Astronautics, apr 1978.

[37] H. R. Kaufman, R. S. Robinson, and D. C. Trock, "Inert gas thruster technology," *Journal of Spacecraft and Rockets*, vol. 20, pp. 77–83, jan 1983.

[38] D. Pedrini, T. Misuri, F. Pagnucci, and M. Andrenucci, "Development of hollow cathodes for space electric propulsion at sitael," *Aerospace, MDPI*, 2017.

[39] M. F. Schatz, "Heaterless ignition of inert gas ion thruster hollow cathodes," in *International Electric Propulsion Conference*, American Institute of Aeronautics and Astronautics, Sep 1985.

[40] L. Mueller, "High reliability cathode heaters for ion thrusters," in *International Electric Propulsion Conference*, AIAA, November 1976.

[41] D. R. Lev, I. G. Mikellides, D. Pedrini, D. M. Goebel, B. A. Jorns, and M. S. McDonald, "Research progress in research and development of hollow cathodes for electric propulsion," *Reviews of Modern Plasma Physics*, April 1999.

[42] B. Rubin and J. Williams, "Hollow cathode conditioning and discharge initiation studies," vol. 1, pp. 662 – 665, 07 2007.

[43] A. Daykin-Iliopoulos, S. Gabriel, I. Golosnoy, K. Kubota, and I. Funaki, "Investigation of heaterless hollow cathode breakdown," in *34th International Electric Propulsion Conference*, July 2015.

[44] V. Vekselman, Y. E. Krasik, S. Gleizer, V. T. Gurovich, A. Warshavsky, and L. RabiNovich, "Characterization of a heaterless hollow cathode," *Journal of Propulsion and Power*, vol. 29, pp. 475–486, Mar 2013.

[45] F. Paschen, "Bohrs heliumlinien," *Annalen der Physik*, vol. 355, no. 16, pp. 901–940, 1916.

[46] N. Koshelev and A. Loyan, "Investigation of hollow cathode for low power hall effect thruster," in *30th International Electric Propulsion Conference*, 2007.

[47] H. Eichhorn, K. H. Schoenbach, and T. Tessnow, "Paschen's law for a hollow cathode discharge," *Applied Physics Letters*, vol. 63, pp. 2481–2483, Nov 1993.

[48] D. M. Goebel and E. Chu, "High-current lanthanum hexaboride hollow cathode for high-power hall thrusters," *Journal of Propulsion and Power*, vol. 30, pp. 35–40, Jan 2014.

[49] J. P. Bojon, D. L. Ngoc, B. Versolatto, and J. Jimenez, "Graphite and c-c materials for uhv applications." CERN LHC Collimation Project, June 2003.

[50] S. J. Hall, T. G. Gray, J. T. Yim, M. Choi, M. M. Mooney, T. R. Sarver-Verhey, and H. Kamhawi, "The effect of anode position on operation of a 25-a class hollow cathode," in *International Electric Propulsion Conference*, September 2019.

[51] D. Pedrini, R. Albertoni, F. Paganucci, and M. Andrenucci, "Experimental characterization of a lanthanum hexaboride hollow cathode for five-kilowatt-class hall thrusters," *Journal of Propulsion and Power*, vol. 32, pp. 1557–1561, Nov 2016.

[52] G.-C. Potrivitu, R. Joussot, and S. Mazouffre, "Anode position influence on discharge modes of a lab_6 cathode in diode configuration," *Vacuum*, vol. 151, pp. 122–132, February 2018.

[53] G. Sary, L. Garrigues, and J.-P. Boeuf, "Hollow cathode modeling: II. physical analysis and parametric study," *Plasma Sources Science and Technology*, vol. 26, p. 055008, Mar 2017.

[54] A. Richardson, *2019 NRL Plamsa Formulary*. U.S. Naval Research Laboratory, 2019.

[55] M. L. Warren, "Development of an annular micro-thruster and halbach permanent magnet arrays in hall-effect thrusters," Master's thesis, The University of Alabama, 2018.

[56] J.-P. Bouef, "Tutorial:physics and modelling of hall thrusters," *Journal of Applied Physics*, vol. 121, 2017.

Appendix A

Cylindrical Hall Thruster with a Halbach array arrangement

Section 2.1 briefly discusses the complex physics behind the working of a Hall thruster. Compared to ion thrusters, Hall thrusters are simple devices and their architecture is discussed in Section A.1. The geometry of the discharge channel and the magnetic field shape govern Hall thruster operation. The following sections discuss the preliminary design and simulation of a low power Hall thruster. This Hall thruster design is referred to as the VTHT. A non-conventional magnetic circuit design consisting of a special arrangement of permanent magnets is utilized instead of the traditional radial field design employed using electromagnets. This work is inspired by the Hall thruster design discussed by Warren in [55]. Complex 3-D computer simulations, required to effectively model an effective thruster and predict its performance, were deemed beyond the scope of this research and will be realized in future.

A.1 Architecture

Figure 2.4 shows the various components necessary for successful Hall thruster operation.

- Cylindrical discharge channel:
  Usually, the discharge channel consists of a dielectric insulating wall. The wall is manufactured from dielectric materials. Dielectric materials are desirable because of their reduced sputtering yield and reduced secondary electron emission coefficients when bomabarded with propellant ions [1], which increases the thruster lifetime. Alternatively, a different version of Hall thruster, called a thruster with anode layer (TAL), employs a metallic conducting wall. This version implements the magnetic shielding technique to resist the sputtering due

to ion bombardment.

- Anode/Gas Inlet:
  The anode is typically positioned near the discharge channel base except for the TAL, where it extends close to the thruster exit [1]. It is made up of stainless steel to be able to endure high temperatures. The anode doubles as the propellant inlet and is designed such that the propellant is dispersed uniformly. An axial electric field develops between the anode and the cathode, creating the Hall-effect force responsible for generating the thrust plume.

- Magnetic circuit:
  Magnetic circuit in a conventional Hall thruster consists of electromagnets and/or ferromagnetic frame. The locations of these components varies for different thruster designs. The radial magnetic field is designed such that it is at its peak near the thruster exit plane and falls close to zero at the anode. Numerous configurations can be employed to achieve a unvaried magnetic field in the thruster channel using the least number of electromagnetic coils to minimize the thruster weight and power requirement.

- Hollow cathode:
  The hollow cathode device produces plasma which acts as the electron source for propellant ionization and provides electrons for ion beam neutralization. Unlike ion thrusters, Hall thrusters require only a single hollow cathode to perform these functions. The electrons from the cathode plume are pulled in the direction of the anode and are eventually trapped (see Figure 2.4). The ExB drift causes the electrons to spiral azimuthally until they impact a neutral propellant atom and ionize it. Additionally, the ions in the thruster plume are neutralized by the electrons discharge from the cathode to prevent charge collection on the surface of the vehicle, resulting in a reduction in the generated change in velocity.

A.2 Hall thruster design

The thruster is designed with the aim of operating in the range of 400-1000 W. Based on the literature for thrusters operating in a similar range, the outside channel radius and thickness is chosen. Goebel and Katz [1] discuss thruster operating principles and scaling laws which are utilized to design the thruster. Bouef [56] provides a detailed explanation for the design of the Stationary plasma thruster 100 (SPT100) thrusters (see Table A.2). The electrical and performance characteristics of the SPT100 along with the thruster scaling laws are utilized to design the thruster.

The electrons from the cathode plume enter the discharge chamber, to be trapped by the radial magnetic field, with a Larmor radius given as[1],

$$r_L = \frac{1}{B}\sqrt{\frac{8m}{\pi e^2}T_{eV}} \tag{A.1}$$

where T_{eV} is assumed as 25 eV. The electron Larmor radius should have a lower value than the height and width of the thruster channel to prevent them from spiralling to the anode and to protect the channel walls from eroding and sputtering due to electron bombardment, respectively. It is also essential that the electrons must be magnetized before resulting in E X B field diffusion due to collision with a neutral or ion, which is normally described by [1]

$$\Omega_e^2 = \frac{\omega_c^2}{\nu^2} >> 1 \tag{A.2}$$

Similarly, the ion Larmor radius should be much greater than the thruster channel length to successfully accelerate the ions using the applied electric field. A feasible magnetic field magnitude is selected such that these criteria are satisfied. Finally, the thruster ionization region size should be sufficient to ensure replenishment of the thruster channel with neutral propellant atoms as the ions are accelerated out, ensuring high propellant utilization. The neutral density in the anode region is calculated as [56],

$$n_a = \frac{\dot{m}}{M}\frac{1}{A_t v_a} \tag{A.3}$$

where v_a is assumed as 250 m/s. Additionally, it has been observed that some of the ionized atoms collide with the channel walls and re-enter as neutral atoms instead of being accelerated out of the thruster. Thus, the plasma thickness is required to be greater than the ionization mean free path to ensure efficient use of propellant [1]. This gives an important thruster scaling law, given as [1],

$$\frac{\lambda_i}{L} = constant << 1 \tag{A.4}$$

The conditions discussed above for successful Hall thruster operation are calculated for the VTHT and found to be satisfied, ensuring a good Hall thruster design (see Table A.1). Note that the discharge current density and magnetic field strength are assumed as 1000 A/m^2 [8] and 0.035 Tesla, respectively.

The thrust and power for a Hall thruster are proportional to the product of the thruster channel length and width [56]. This information along with the thruster laws were employed using a MatLab code to calculate the thruster dimension and performance characteristics, shown in Table A.2.

Parameter	Value
Electron Larmor radius (cm)	0.054
Ion Larmor radius (cm)	68
Neutral density near the anode region (m^{-3})	3.63 x 10^{19}
Electron density (m^{-3})	3.3 x 10^{17}
Ion density (m^{-3})	2.3 x 10^{17}
Ionization mean free path (cm)	1.86
Krypton mass flow rate (mg/s)	2.6

Table A.1: Thruster operation parameters for the VTHT

Parameters	SPT100	VTHT
Discharge current (A)	4.5	2
Discharge voltage (V)	300	325
Power (W)	1350	666
Thrust (mN)	90.2	0.044
Specific impulse (s)	1734	1734
Channel length (cm)	2.5	2.54
Inner channel radius (cm)	3.5	1.27
Outer channel radius (cm)	5	2.8

Table A.2: Comparison of thruster parameters for SPT100 and VTHT

A.3 Halbach array

One main advantage of utilizing permanents magnets to produce a steady magnetic field to trap electrons and generate the Hall effect is the significant decrease in electric power consumption. This enables the Hall thruster technology to be used for long term space missions, where power source is a limiting factor. For this purpose a permanent magnet assembly called Halbach array is used in this Hall thruster design.

In a Halbach array, the permanents magnets are arranged such that the magnetization has a spatially rotating pattern. The magnetization pattern elevates the magnetic field on one side of the array and reduces the field to zero on the other side. These magnets can be arranged in a linear or cylindrical fashion, based on the application. This work uses a Halbach cylinder due

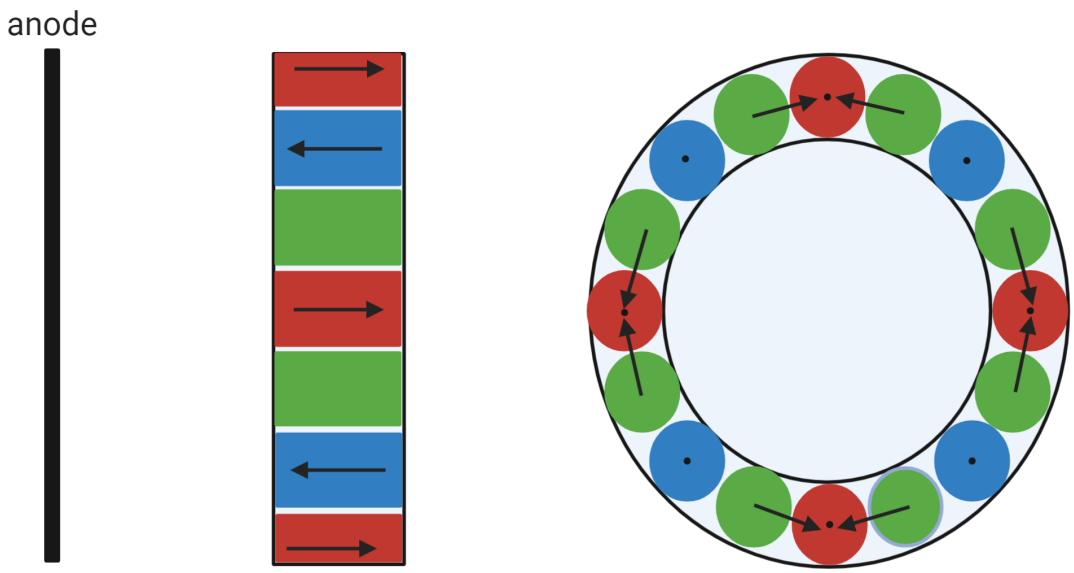

Figure A.1: Schematic of the Halbach array. The left part is a side view of the Halbach array showing the axial magnetization while the right part is a top view showing the diametric magnetization

to the cylindrical asymmetric structure of a Hall thruster device. Ideally, in an infinite length Halbach cylinder, the augmented field is restricted within the cylinder with zero field outside, which can increase the thruster efficiency. In practise the finite length of the cylinder introduces non-uniformities in the field.

A permanent magnet used in a Hall thruster is required to withstand high temperatures and the environment in space. Additionally, high magnetic strength and resistance to demagnetization are required to ensure long thruster lifetimes. Based on these requirements, readily available permanent magnet sizes and the Hall thruster dimensions, samarium cobalt (SmCo) magnets are selected to design a laboratory model of the Hall thruster.

To simulate and understand the behavior of the Halbach array with Hall thruster geometry, inspiration is drawn from the work [55] carried out at the University of Alabama, and a similar Halbach arrangement is used. The aim is to carry out further improvements and changes in the arrangement based on the preliminary results from the simulation. The cylindrical magnets are arranged such that the magnetization direction is: axially towards the anode, axially away from the anode, and circumferentially towards the next magnet. Figure A.1 shows the arrangement, where the red stands for axially magnetized magnets with the north pole pointed away from the anode, blue stands for axially magnetized magnets with the north pole pointed towards the anode, and green stands for diametrically magnetized magnets such that the north pole faces the nearest red magnet, across a line connecting the two magnet's centers. The complex 3D field produced by

the Halbach cylinder requires a 3D electromagnetic simulator to model all the components of the magnetic field.

While the time and effort required to achieve successful simulations are beyond the scope of the presented work, it is the hope of the author that future electric propulsion efforts at Virginia Tech will continue to carry out these simulations and validate the usability of Halbach arrays with Hall thruster technology to enable efficient and long term missions.